CHAPTER 3

Cholesterol functionalized azo-based biphenyl liquid crystals

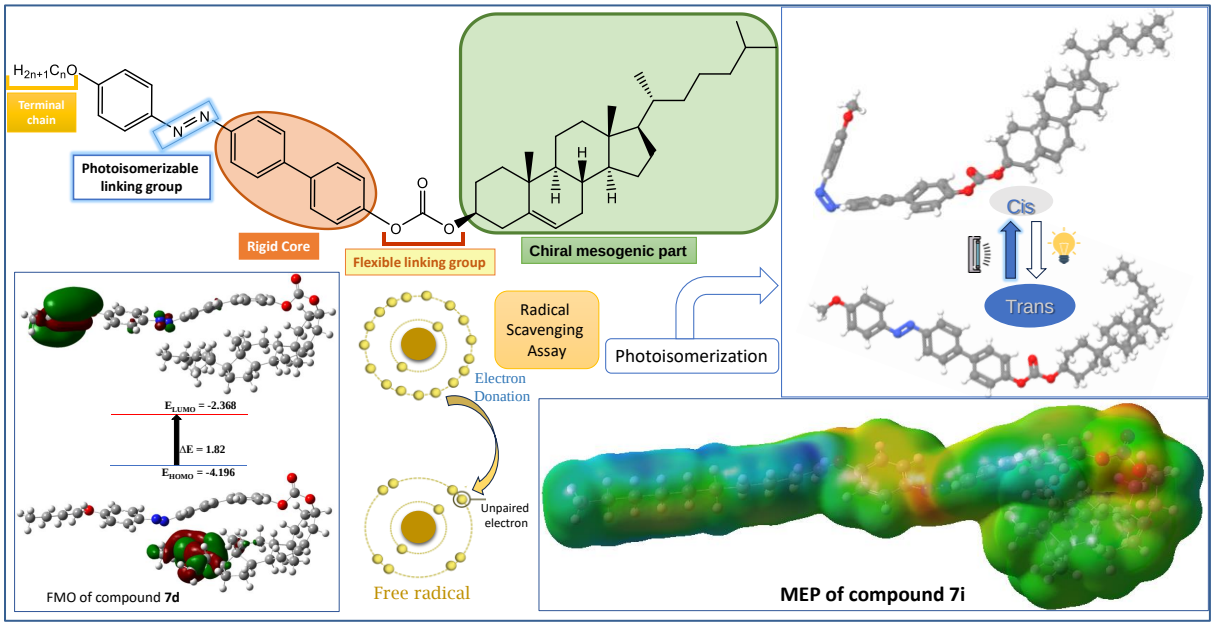

3.1. Introduction

Over the past few years, there has been a rising curiosity for LC based on cholesterol[1]. This is primarily attributed to the existence of chiral centres in cholesterol, leading to the formation of helical supramolecular structures that give rise to some interesting properties of these liquid crystals. One of the important properties of these LCs is their response to external stimuli such as temperature, electric field, pressure, etc., which makes these compounds gainful for various applications including colour displays, fast response displays, optical storages, selective reflection, optical switching, etc. [2–4]. Also, cholesterol-based compounds have a wide range of application ranging from drug delivery or bioimaging applications to cholesterol-based liquid crystal and gelators, as well as purely synthetic applications [5].

Chirality has significant effect on the mesophase structures of liquid crystals, leading to a diverse range of mesophases, including chiral nematic, twist grain boundary, chiral smectic and cubic blue phase. Each of these phases exhibits unique and distinctive properties [6]. Among the diverse cholesterol-based mesogens, the rod-shaped dimers predominantly feature symmetric or unsymmetric groups, incorporate a cholesterol group interconnected with various types of linking units, including phenyl, biphenyl, Schiff base (-CH=N), chalcone (-CO-CH=CH-), ester (-COO-), and azo group (-N=N-) etc. supported by central and/or terminal alkyl chains [7–10]. The choice of a linking group has the potential to impact both the overall molecular length and the polarisable anisotropy of the mesogen, offering a favourable molecular geometry. Azobenzene, serving as a linking group, exhibits thermal stability and is capable of undergoing photo-induced reversible isomerisation under UV irradiation [10,11]. The trans-form of azobenzene possesses a rod-like structure that contributes to the stabilization of the liquid crystal superstructure. Conversely, its cis-form adopts a bent-like structure, typically leading to the destabilisation of the liquid crystal superstructure by inducing disorder in the aligned systems [12]. Hence, the azobenzene moiety stands as the most commonly employed photoactive bistable group in the designing of liquid crystals.

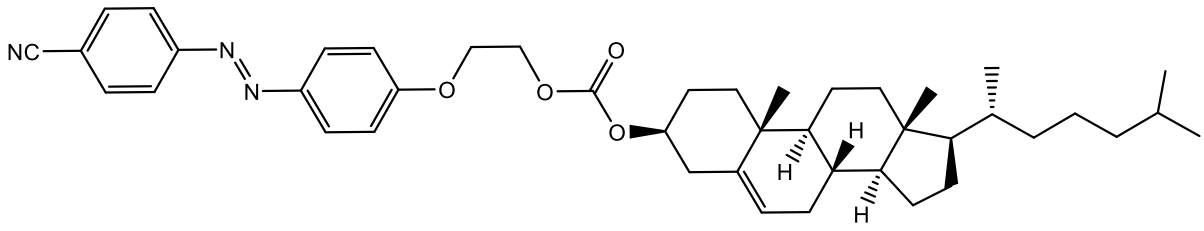

(a)

Figure 3.1 (a): Cholesterol-azobenzene liquid crystal containing carbonate linkage

Tan et al. [13], synthesized cholesterol-azobenzene liquid crystal containing carbonate linkage and CN terminal group **(Figure 3.1 (a))**, showing chiral nematic (N*) and chiral smectic C (SmC*) phases. This compound exhibited reversible photoresponsive chiral liquid crystal properties, capable of forming multistimuli responsive organogels in organic solvents. It demonstrated photoresponsive behaviour in solution, liquid crystal and the gel state.

George et al. [14], reported number of cholesterol-based liquid crystalline derivatives with azo-carbonate linkages **(Figure 3.1 (b))**. The compounds exhibited cholesteric, Smectic A and TGB_A mesophases. These compounds acquire photochromic properties due to the presence of an azobenzene group.

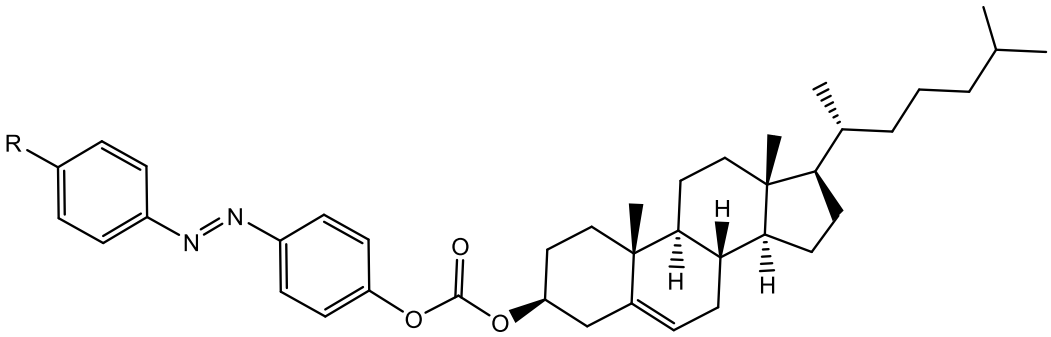

where R= H, NO_2, $N(CH_3)_2$, *n*-C_4H_9

(b)

Figure 3.1 (b): Cholesterol-based liquid crystalline derivatives with azo-carbonate linkages

Gupta et al. [15], synthesized eight oligomeric azobenzene centred cholesterol-based tetramers with varying flexible alkyl spacers **(Figure 3.1 (c))**. Compounds exhibited monotropic, enantiotropic cholesteric mesophase and displayed photoisomerization in dilute solutions.

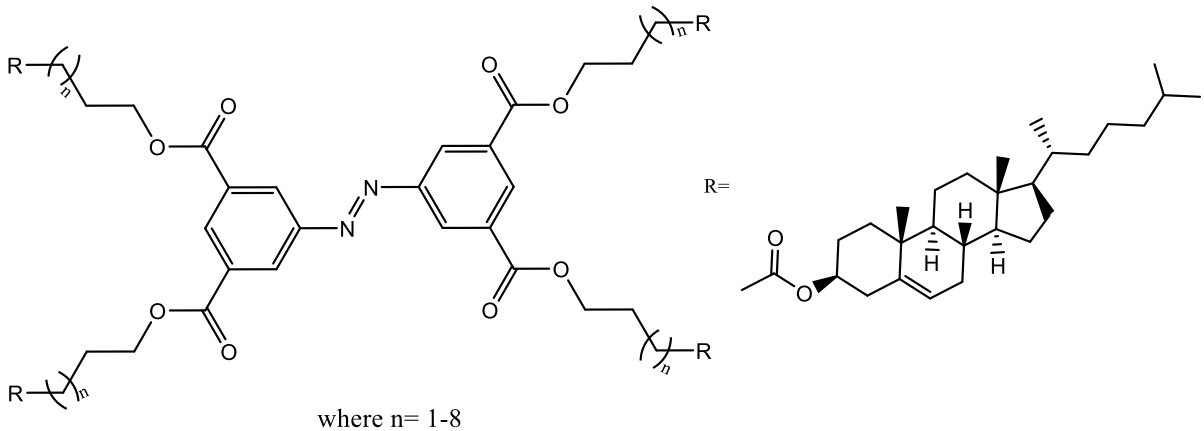

where n= 1-8

(c)

Figure 3.1 (c): Oligomeric azobenzene centred cholesterol-based tetramers

Mali et al. [16], have synthesized four compounds with cholesteryl group, azo-ester linking group and two-side substituted flexible alkoxy side chains **(Figure 3.1 (d))**. All compounds displayed smectic A mesophase with broad temperature range. The photoresponsive behaviour of these compounds were also studied.

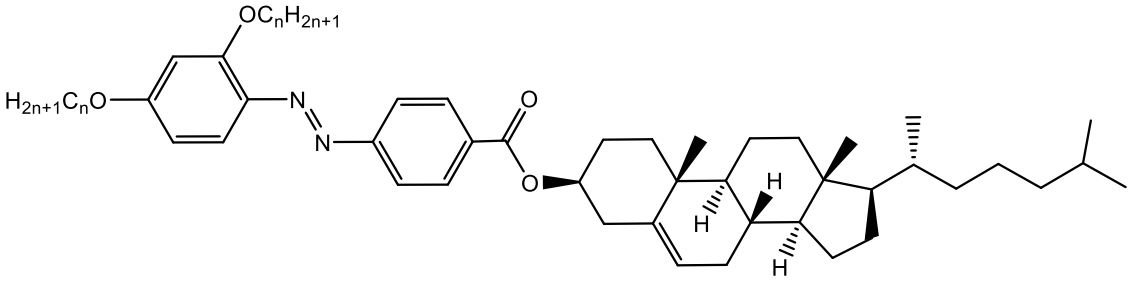

where n= 10, 12, 16 & 18

(d)

Figure 3.1 (d): LC with cholesteryl group and azo-ester linkage

Also, many cholesterol-based liquid crystal monomers, dimers, trimers, tetramers, polymers etc. have been reported showing various types of mesophases including cholesteric or chiral nematic, smectic A, smectic C*, twist grain boundaries, blue phases, etc. [7,13,17–28].

The ongoing exploration of designing and synthesizing novel cholesteric liquid crystals (CLCs) with responsive functionalities and investigating their unique physical properties remains an attractive subject in LC field.

In the present study, we have synthesized a new homologous series of cholesterol-bearing liquid crystals featuring azo-carbonate linkages, a biphenyl moiety and terminal alkoxy groups, with the alkyl chain lengths systematically varying from methyl to n-octadecyl. The mesomorphic characteristics of these cholesteric liquid crystals (CLCs) were examined using DSC and POM. The UV spectrum was employed to study the photo-switching properties. The structure-property relationship of present liquid crystalline derivatives was discussed to investigate the scope of mesogenic properties.

3.2. Experimental

3.2.1. Materials

Cholesteryl chloroformate was purchased from Sigma-Aldrich Chemicals, USA. 1,1-diphenyl-2-picrylhydrazyl (for antioxidant assay) was purchased from TCI Chemicals, Japan. Paracetamol, potassium carbonate, alkyl bromides, sodium nitrite, 4-hydroxy biphenyl, sodium hydroxide, pyridine and other reagents were purchased from Loba Chemie Pvt. Ltd., India.

Tetrahydrofuran (THF), acetone, methanol and ethanol underwent drying treatment with standard methods. All remaining solvents and reagents were of AR grade and used without additional purification.

3.2.2. Techniques and measurements

The compounds' structures were established using standard spectroscopic techniques. The process of thin-layer chromatography (TLC) was conducted using silica gel plates manufactured by Merck. The FT-IR spectra were obtained using a Bruker spectrometer with KBr pellets. The spectrum data for ^{1}H NMR and ^{13}C NMR were obtained using an Avance Bruker 400 spectrometer (400 MHz). Deuterated chloroform ($CDCl_3$) was used as the solvent, and TMS was used as an internal standard. The polarised optical microscopy (POM) analysis was conducted using a Nikon Eclipse Ci-Pol microscope that was fitted with a Linkam (Linkam, Surrey, England) heating stage. The phase transition temperatures and thermodynamic parameters were obtained using differential scanning calorimetry (DSC-822, Mettler Toledo, using Stare software). The rates of heating and cooling were 10°C per minute. The apparatus underwent calibration using indium as a reference standard. The thermal stability of the compounds was assessed using a thermogravimetry analyser (TGA-50, Shimadzu, Japan) with a sample size of 3-7 mg placed in a platinum pan. The heating rate was set at 10°C/min. The elemental analysis were conducted using Thermo Finnigan's CHN analyser from the Flash 1112 series. The Shimadzu UV-1800 spectrometer (Japan) was used to measure absorbance. Gaussian 09, revision A.02 software was utilized for DFT calculations.

3.2.3. Synthesis and characterisation

The synthetic routes of the mesogenic Schiff's base are shown in **Scheme 3.1**.

*3.2.3.1. Synthesis of 4-n-alkoxy acetanilide **(2 a-m)***

In a 100 ml three-necked round-bottom flask, a mixture of paracetamol (0.1 mol) **(1)**, anhydrous potassium carbonate (0.15 mol), and dry acetone (60 ml) was taken. The reaction mixture underwent heating to 70-80°C with stirring. Subsequently, the appropriate alkyl bromide (0.15 mol) was added dropwise over 1 h to the warm solution. The resulting mixture was then refluxed with continuous stirring at 70-80°C for 8-12 h. After cooling to room temperature, the mixture was diluted with cold water. The solid mass obtained underwent filtration, washing with water and was directly utilized for hydrolysis [17]. Yield: 80-90%.

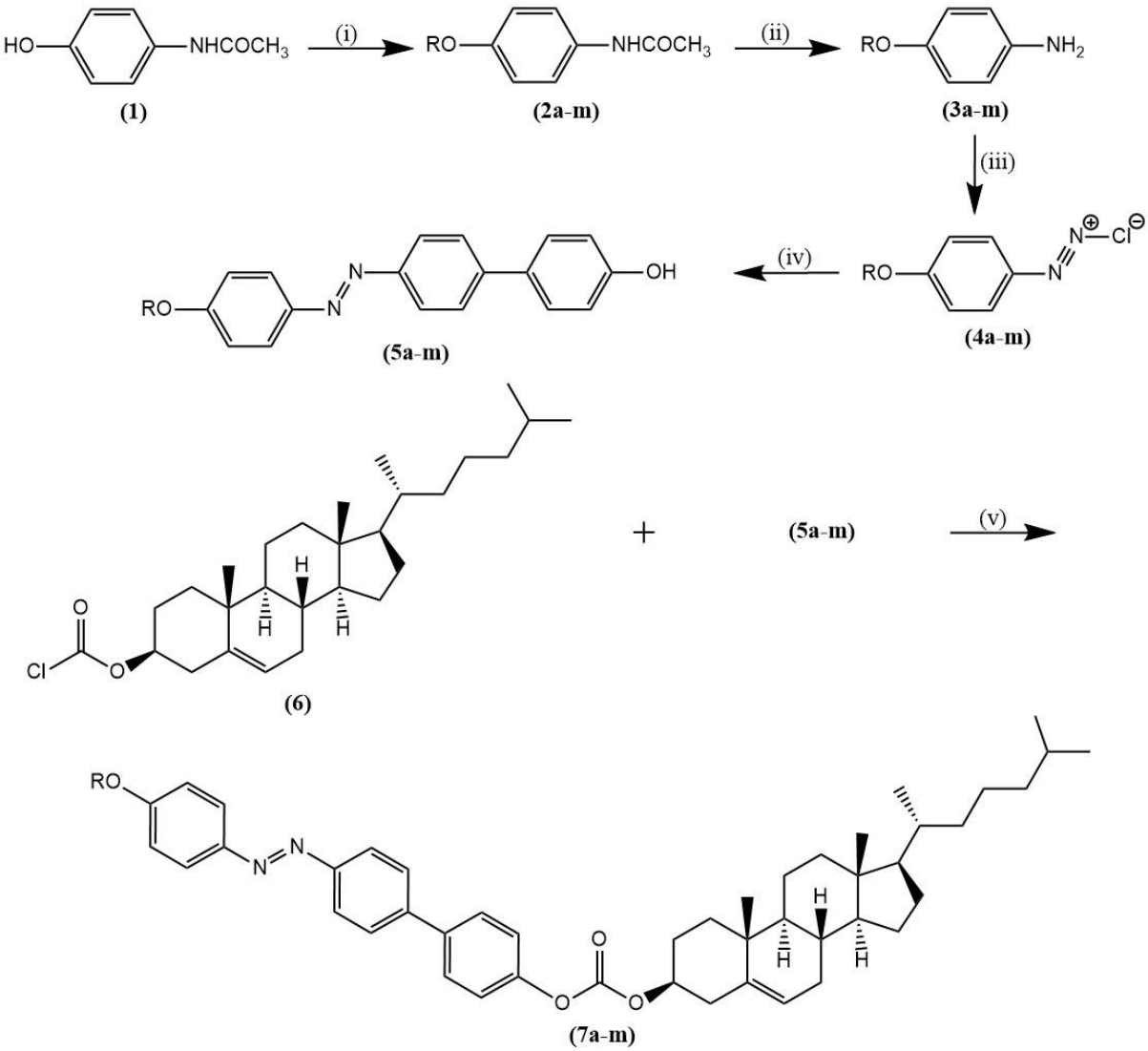

R=C_nH_{2n+1}, n= 1 to 8, 10, 12, 14, 16 and 18

Scheme 3.1: Synthetic route for final derivatives (7a-m). Reagents and conditions; (i) n-alkyl bromide, dry acetone, anhydrous K_2CO_3, reflux for 8-10 h, (ii) 50% hydrochloric acid, 90-95°C, 10-12 h, (iii) conc. HCl, $NaNO_2$, 0–5°C, (iv) 4-hydroxy biphenyl, 10% NaOH solution, 0–5°C, 3-4 h, (v) dry THF, pyridine, stirring, 38-40°C, 3-4 h.

*3.2.3.2. Synthesis of 4-n-alkoxy aniline **(3 a-m)***

A mixture of 4-n-alkoxy acetanilide (0.014 mol) **(2 a-m)**, water (7 ml) and concentrated hydrochloric acid (4.5 ml) was stirred for 10 to 12 h at 90-95°C and then cooled to room temperature. The mixture was made alkaline with 50% sodium hydroxide solution at 20°C. The oily/waxy product was extracted with diethyl ether. After evaporation of solvent on a rotary evaporator the corresponding products were obtained as pale-yellow oils and higher member were obtained as light brown solids. Boiling/melting point agrees with the reported value [29]. Yield: 75-80%.

*3.2.3.3. Synthesis of 4-n-alkoxy diazonium chloride **(4 a-m)***

In a beaker, alkoxy aniline (0.005 mol) **(3a-m)** was mixed with 50 ml of water and cooled to 0–5°C using an ice bath. Subsequently, concentrated HCl (0.03 mol) was added, and the reaction mixture was stirred for 1 h. A solution of $NaNO_2$ (0.005 mol) in 5 ml of pre-cooled water at 0°C was then added over 5 minutes with continuous stirring. The solution was stirred for an additional hour. At this point, Congo red paper and starch iodide paper both exhibited a positive test for the presence of nitrous acid, indicated by a blue color. Sulfamic acid was added to remove excess nitrous acid. After this step, Congo red paper continued to show a positive test (blue color), while starch iodide paper displayed a negative test. The resulting diazonium salt was obtained as a clear solution and utilized for subsequent coupling reactions [30].

*3.2.3.4. Synthesis of 4'-(4-n-alkoxyphenyl) diazenyl-1,1'-biphenyl-4''-ol **(5 a-m)***

A well-stirred solution of 4-hydroxy biphenyl (0.005 mol) in 60 ml of water was gradually treated with alkoxy aniline diazonium chloride **(4 a-m)** over 1 h at 0°C–5°C. The pH was maintained at 7.0 by adding a 10% w/v NaOH solution. For an additional 3–4 h the stirring was continued to ensure complete separation, and the resulting dye was isolated through filtration, washed with water, dried, and subsequently crystallized from ethyl acetate, yielding reddish-brown crystals. The overall yield was approximately 70-85%. Melting points/transition temperature agrees well with the reported values [30].

*3.2.3.5. Synthesis of 4'-(4-n-alkoxyphenyl) diazenyl-1,1'-biphenyl-4''-cholesteryl carbonate **(7 a-m)***

Cholesteryl chloroformate (0.01 mol) **(6)** was combined with dry THF (50 ml) in a quick-fit RBF. To this mixture, compound **(5a-m)** (0.011 mol), dry THF (40 ml), and anhydrous pyridine (4.0 ml) as a proton scavenger were added. The resulting mixture was stirred at approximately 38-40°C for 3-4 h with an attached guard tube. Subsequently, the mixture was filtered to separate pyridinium chloride and other insoluble materials. The filtrate was then concentrated under vacuum to remove excess THF. Following this, n-hexane was added for reprecipitation, and the mixture underwent filtration once again. The resulting precipitate was further recrystallized from an ethyl acetate-methanol mixture (60:40) until a consistent transition temperature was achieved.

Compound 7a: Yellow crystalline solid, yield: 82.6%, IR (KBr, ν_{max} , cm^{-1}): 3037, 2949, 2901, 2854, 1757, 1597, 1521, 1487, 1255, 835; ^{1}H-NMR ($CDCl_3$, 400 MHz): δ(ppm) =

δ7.01-8.25 (m, 12 H, Ar-H), δ5.46 (m, 1H, -C=CH-), δ4.6 (m, 1H -OCH-CH_2), δ3.91 (s, 3H, -OCH_3), δ2.54-2.58 (m, 2H, -OCH-CH_2), δ2.05-0.70 (m for 41H, -CH, -CH_2 and -CH_3); ^{13}C NMR ($CDCl_3$, 400 MHz): δ(ppm) = 162.8, 152.3 (>C=O; carbonate) , 150.2, 150.0, 145.0, 140.8, 139.4, 137.6, 131.8, 131.0, 126.7, 126.2, 124.8, 122.3, 121.9, 114.6, 76.82, 56.78, 56.18, 50.15, 42.44, 40.2, 39.54, 37.27, 31.95, 31.68, 28.25, 28.03, 26.52, 26.21, 25.81, 24.31, 23.86, 23.55, 22.84, 22.58, 21.95, 21.10, 21.07, 19.41, 18.73, 11.87; Elemental analysis: calculated for $C_{47}H_{60}N_2O_4$(%): C, 78.73; H, 8.44; N, 3.91; found: C, 78.41, H; 8.76; N; 4.28.

Compound 7b: Yellow crystalline solid, yield: 77.5%, IR (KBr, ν $_{max}$, cm^{-1}): 3036, 2954, 2896, 2845, 1754, 1588, 1508, 1487, 1256, 835; ^{1}H-NMR ($CDCl_3$, 400 MHz): δ(ppm) = δ7.07-8.18 (m, 12 H, Ar-H), δ5.46 (m, 1H, -C=CH-), δ4.56 (m, 1H -OCH-CH_2), δ4.06 (m, 2H, -OCH_2CH_3), δ2.52-2.56 (m, 2H, -OCH-CH_2), δ2.05-0.70 (m for 44H, -CH, -CH_2 and -CH_3); ^{13}C NMR ($CDCl_3$, 400 MHz): δ(ppm) = 159.68, 152.32 (>C=O; carbonate) , 150.2, 150.0, 145.02, 140.82, 137.6, 131.8, 131.0, 128.6, 126.7, 126.2, 124.8, 122.3, 121.9, 114.6, 78.20, 66.68, 56.78, 56.18, 50.14, 42.45, 40.21, 39.53, 37.27, 31.94, 31.53, 28.34, 28.01, 26.74, 26.43, 25.80, 24.32, 23.87, 23.56, 22.77, 22.34, 21.90, 21.06, 21.00, 19.42, 18.68, 14.75, 11.88; Elemental analysis: calculated for $C_{48}H_{62}N_2O_4$(%): C, 78.86; H, 8.55; N, 3.83; found: C, 78.49; H, 8.22; N, 3.65.

Compound 7c: Yellow crystalline solid, yield: 78.6%, IR (KBr, ν $_{max}$, cm^{-1}): 3046, 2950, 2870, 2846, 1757, 1590, 1514, 1442, 1248, 844; ^{1}H-NMR ($CDCl_3$, 400 MHz): δ(ppm) = δ7.06-8.18 (m, 12 H, Ar-H), δ5.46 (m, 1H, -C=CH-), δ4.57 (m, 1H -OCH-CH_2), δ4.02 (m, 2H, -OCH_2CH_3), δ2.50-2.56 (m, 2H, -OCH-CH_2), δ2.05-0.70 (m for 46H, -CH, -CH_2 and -CH_3); ^{13}C NMR ($CDCl_3$, 400 MHz): δ(ppm) = 160.54, 152.30 (>C=O; carbonate) , 150.21, 150.04, 145.02, 143.08, 140.81, 137.68, 131.82, 131.04, 128.68, 126.72, 126.26, 124.81, 122.34, 121.98, 114.60, 78.22, 69.33, 56.70, 56.17, 50.12, 42.45, 40.21, 39.53, 37.26, 31.94, 31.53, 28.34, 28.01, 26.74, 26.43, 25.80, 24.32, 23.87, 23.56, 22.68, 22.17, 21.90, 21.06, 21.00, 19.42, 18.68, 14.75, 11.86; Elemental analysis: calculated for $C_{49}H_{64}N_2O_4$(%): C, 78.99; H, 8.66; N, 3.76; found: 78.72; H, 8.39; N, 3.56.

Compound 7d: Yellow crystalline solid, yield: 85.2%, IR (KBr, ν $_{max}$, cm^{-1}): 3041, 2944, 2862, 2847, 1756, 1588, 1514, 1444, 1242, 842; ^{1}H-NMR ($CDCl_3$, 400 MHz): δ(ppm) = δ7.01-8.18 (m, 12 H, Ar-H), δ5.46 (m, 1H, -C=CH-), δ4.57 (m, 1H -OCH-CH_2), δ4.00 (m, 2H, -OCH_2CH_3), δ2.50-2.56 (m, 2H, -OCH-CH_2), δ2.05-0.70 (m for 48H, -CH, -CH_2 and -CH_3); ^{13}C NMR ($CDCl_3$, 400 MHz): δ(ppm) = 160.54, 152.32 (>C=O; carbonate) , 150.21, 150.04, 145.02, 143.10, 140.80, 137.68, 131.82, 131.04, 128.68, 126.72, 126.28, 124.81, 122.37, 121.98, 114.60, 78.22, 68.40, 56.70, 56.17, 50.12, 42.45, 40.21, 39.53, 37.26, 31.94, 31.80,

31.58, 28.36, 28.04, 26.78, 26.44, 25.82, 24.31, 23.84, 23.55, 22.67, 22.15, 21.94, 21.18, 21.00, 19.42, 19.00, 18.68, 14.12, 12.00; Elemental analysis: calculated for $C_{50}H_{66}N_2O_4$(%): C, 79.11; H, 8.76; N, 3.69; found: C, 78.87; H, 8.48; N, 3.55.

Compound 7e: Yellow crystalline solid, yield: 82.8%, IR (KBr, ν_{max} , cm^{-1}): 3038, 2944, 2860, 2841, 1750, 1580, 1506, 1442, 1240, 846; ^{1}H-NMR ($CDCl_3$, 400 MHz): δ(ppm) = δ7.01-8.17 (m, 12 H, Ar-H), δ5.46 (m, 1H, -C=CH-), δ4.57 (m, 1H -OC<u>H</u>-CH_2), δ4.06 (m, 2H, -OC<u>H_2</u>CH_3), δ2.50-2.54 (m, 2H, -OCH-C<u>H_2</u>), δ2.05-0.70 (m for 50H, -CH, -CH_2 and -CH_3); ^{13}C NMR ($CDCl_3$, 400 MHz): δ(ppm) = 160.55, 152.32 (>C=O; carbonate) , 150.22, 150.04, 145.02, 143.10, 140.80, 137.70, 131.88, 131.17, 128.68, 126.72, 126.28, 124.82, 122.38, 121.99, 114.62, 78.22, 68.70, 56.78, 56.22, 50.12, 42.45, 40.24, 39.53, 37.26, 31.96, 31.75, 31.53, 29.32, 28.47, 28.11, 26.80, 26.42, 25.82, 24.31, 23.84, 23.55, 22.72, 22.16, 21.94, 21.18, 21.00, 19.52, 19.04, 18.68, 14.10, 12.00; Elemental analysis: calculated for $C_{51}H_{68}N_2O_4$(%): C, 79.23; H, 8.87; N, 3.62; found: C, 79.20; H, 8.58; N, 3.70.

Compound 7f: Yellow crystalline solid, yield: 83.4%, IR (KBr, ν_{max} , cm^{-1}): 3035, 2946, 2868, 2844, 1756, 1579, 1506, 1442, 1242, 844; ^{1}H-NMR ($CDCl_3$, 400 MHz): δ(ppm) = δ7.00-8.17 (m, 12 H, Ar-H), δ5.46 (m, 1H, -C=CH-), δ4.57 (m, 1H -OC<u>H</u>-CH_2), δ4.06 (m, 2H, -OC<u>H_2</u>CH_3), δ2.50-2.54 (m, 2H, -OCH-C<u>H_2</u>), δ2.05-0.70 (m for 52H, -CH, -CH_2 and -CH_3); ^{13}C NMR ($CDCl_3$, 400 MHz): δ(ppm) = 161.12, 152.32 (>C=O; carbonate) , 150.22, 150.04, 145.02, 143.10, 140.80, 137.70, 131.86, 131.23, 128.68, 126.77, 126.30, 124.80, 122.38, 121.99, 114.62, 78.30, 68.70, 56.78, 56.22, 50.12, 42.45, 40.25, 39.54, 37.28, 31.91, 31.85, 31.63, 31.46, 29.35, 28.55, 28.23, 26.85, 26.48, 25.82, 24.32, 23.95, 23.58, 22.77, 22.16, 21.90, 21.36, 21.03, 19.54, 19.08, 18.66, 14.10, 12.00; Elemental analysis: calculated for $C_{52}H_{70}N_2O_4$(%): C, 79.35; H, 8.96; N, 3.56; found: C, 79.03; H, 8.78; N, 3.80.

Compound 7g: Yellow crystalline solid, yield: 77.2%, IR (KBr, ν_{max} , cm^{-1}): 3031, 2940, 2872, 2848, 1756, 1578, 1506, 1441, 1250, 838; ^{1}H-NMR ($CDCl_3$, 400 MHz): δ(ppm) = δ6.98-8.16 (m, 12 H, Ar-H), δ5.47 (m, 1H, -C=CH-), δ4.57 (m, 1H -OC<u>H</u>-CH_2), δ4.06 (m, 2H, -OC<u>H_2</u>CH_3), δ2.50-2.56 (m, 2H, -OCH-C<u>H_2</u>), δ2.05-0.70 (m for 54H, -CH, -CH_2 and -CH_3); ^{13}C NMR ($CDCl_3$, 400 MHz): δ(ppm) = 161.04, 152.31 (>C=O; carbonate) , 150.24, 150.08, 145.02, 143.10, 140.82, 137.70, 131.89, 131.28, 128.68, 126.74, 126.23, 124.80, 122.38, 121.97, 114.62, 78.32, 68.70, 56.78, 56.22, 50.12, 42.45, 40.28, 39.65, 37.28, 31.94, 31.82, 31.57, 31.39, 29.60, 29.20, 28.68, 28.30, 26.88, 26.43, 25.90, 24.32, 23.94, 23.53, 22.82, 22.25, 21.93, 21.39, 21.06, 19.55, 19.08, 18.66, 14.10, 12.00; Elemental analysis: calculated for $C_{53}H_{72}N_2O_4$(%): C, 79.46; H, 9.06; N, 3.50; found: C, 79.09; H, 8.91; N, 3.71.

Compound 7h: Yellow crystalline solid, yield: 76.8%, IR (KBr, ν_{max} , cm^{-1}): 3042, 2956, 2888, 2843, 1754, 1576, 1508, 1436, 1247, 840; ^{1}H-NMR ($CDCl_3$, 400 MHz): δ(ppm) = δ7.07-8.10 (m, 12 H, Ar-H), δ5.46 (m, 1H, -C=CH-), δ4.54 (m, 1H -OC<u>H</u>-CH_2), δ4.06 (m, 2H, -O<u>C</u>H_2CH_3), δ2.50-2.54 (m, 2H, -OCH-C<u>H</u>$_2$), δ2.05-0.70 (m for 56H, -CH, -CH_2 and -CH_3); ^{13}C NMR ($CDCl_3$, 400 MHz): δ(ppm) = 161.14, 152.31 (>C=O; carbonate) , 150.25, 150.08, 145.02, 143.10, 140.82, 137.70, 131.90, 131.34, 128.68, 126.79, 126.30, 124.80, 122.38, 121.97, 114.62, 78.32, 68.70, 56.78, 56.22, 50.12, 42.45, 40.28, 39.65, 37.28, 31.94, 31.82, 31.57, 31.39, 29.67, 29.64, 29.30, 28.66, 28.27, 26.92, 26.55, 25.90, 24.32, 23.98, 23.67, 22.80, 22.31, 21.88, 21.34, 21.06, 19.56, 19.04, 18.66, 14.10, 12.00; Elemental analysis: calculated for $C_{54}H_{74}N_2O_4$(%): C, 79.56; H, 9.15; N, 3.44; found: C, 79.22; H, 9.00; N, 3.65.

Compound 7i: Yellow crystalline solid, yield: 77.5%, IR (KBr, ν_{max} , cm^{-1}): 3064, 2951, 2922, 2850, 1748, 1604, 1512, 1473, 1255, 833; ^{1}H-NMR ($CDCl_3$, 400 MHz): δ(ppm) = δ6.89-8.18 (m, 12 H, Ar-H), δ5.46 (m, 1H, -C=CH-) δ4.60 (m, 1H -OC<u>H</u>-CH_2), δ4.06 (t, 2H, -O<u>C</u>H_2-CH_2-), δ2.54-2.58 (m, 2H, -OCH-C<u>H</u>$_2$), δ1.18-0.86 (m for 60H, -CH, -CH_2 and -CH_3); ^{13}C NMR ($CDCl_3$, 400 MHz): δ(ppm) = 161.16, 152.14 (>C=O; carbonate) , 150.21, 150.04, 144.30, 142.13, 140.81, 137.68, 131.17, 130.77, 128.86, 126.96, 126.63, 124.11, 122.33, 121.72, 115.10, 79.08, 68.50, 56.78, 56.18, 50.15, 42.45, 42.33, 39.72, 31.88, 31.65, 31.33, 31.11, 29.80, 29.54, 29.40, 29.22, 28.08, 27.27, 26.52, 25.99, 25.81, 24.31, 23.86, 22.84, 22.63, 22.58, 21.10, 19.41, 18.74, 14.11, 11.87; Elemental analysis: calculated for $C_{56}H_{78}N_2O_4$(%): C, 79.76; H, 9.32; N, 3.32; found: C, 79.98; H, 9.07; N, 3.12.

Compound 7j: : Yellow crystalline solid, yield: 80.5%, IR (KBr, ν_{max} , cm^{-1}): 3068, 2949, 2935, 2840, 1749, 1606, 1518, 1472, 1256, 836; ^{1}H-NMR ($CDCl_3$, 400 MHz): δ(ppm) = δ6.89-8.19 (m, 12 H, Ar-H), δ5.46 (m, 1H, -C=CH-) δ4.60 (m, 1H -OC<u>H</u>-CH_2), δ4.06 (t, 2H, -O<u>C</u>H_2-CH_2-), δ2.52-2.57 (m, 2H, -OCH-C<u>H</u>$_2$), δ1.17-0.88 (m for 64H, -CH, -CH_2 and -CH_3); ^{13}C NMR ($CDCl_3$, 400 MHz): δ(ppm) = 161.14, 152.11 (>C=O; carbonate) , 150.20, 150.04, 144.32, 142.11, 140.82, 137.66, 131.18, 130.75, 128.86, 126.94, 126.62, 124.12, 122.30, 121.78, 115.12, 79.08, 68.52, 56.76, 56.20, 50.14, 42.44, 42.32, 39.71, 31.87, 31.63, 31.31, 31.12, 29.93, 29.81, 29.60, 29.54, 29.40, 29.22, 29.04, 28.07, 27.29, 26.64, 25.96, 25.74, 24.36, 23.87, 22.78, 22.59, 22.45, 21.12, 19.44, 18.69, 14.12, 11.88; Elemental analysis: calculated for $C_{58}H_{82}N_2O_4$(%): C, 79.95; H, 9.49; N, 3.22; found: C, 80.12; H, 9.28; N, 3.53.

Compound 7k: Yellow crystalline solid, yield: 80.0%, IR (KBr, ν_{max} , cm^{-1}): 3042, 2958, 2924, 2846, 1752, 1605, 1512, 1476, 1248, 844; ^{1}H-NMR ($CDCl_3$, 400 MHz): δ(ppm) = δ6.91-8.16 (m, 12 H, Ar-H), δ5.46 (m, 1H, -C=CH-) δ4.60 (m, 1H -OC<u>H</u>-CH_2), δ4.06 (t, 2H, -O<u>C</u>H_2-CH_2-), δ2.50-2.56 (m, 2H, -OCH-C<u>H</u>$_2$), δ1.19-0.87 (m for 68H, -CH, -CH_2 and -CH_3);

^{13}C NMR ($CDCl_3$, 400 MHz): δ(ppm) = 161.10, 152.12 (>C=O; carbonate) , 150.22, 150.08, 144.30, 142.18, 140.86, 137.64, 131.16, 130.72, 128.88, 126.93, 126.64, 124.12, 122.31, 121.77, 115.14, 79.08, 68.58, 56.73, 56.23, 50.12, 42.48, 42.31, 39.71, 31.98, 31.77, 31.63, 31.43, 31.32, 31.16, 29.93, 29.82, 29.63, 29.54, 29.43, 29.36, 29.21, 29.18, 29.09, 28.08, 27.26, 26.66, 25.89, 25.68, 24.37, 23.82, 22.75, 22.46, 22.38, 21.14, 19.44, 18.71, 14.10, 11.86; Elemental analysis: calculated for $C_{60}H_{86}N_2O_4$(%): C, 80.13; H, 9.64; N, 3.11; found: C, 80.31; H, 9.39; N, 3.48.

Compound 7l: Yellow crystalline solid, yield: 82.4%, IR (KBr, ν $_{max}$, cm^{-1}): 3044, 2957, 2920, 2838, 1754, 1606, 1514, 1476, 1248, 840; ^{1}H-NMR ($CDCl_3$, 400 MHz): δ(ppm) = δ6.96-8.18 (m, 12 H, Ar-H), δ5.46 (m, 1H, -C=CH-) δ4.60 (m, 1H -OC<u>H</u>-CH_2), δ4.08 (t, 2H, -OC<u>H_2</u>-CH_2-), δ2.52-2.56 (m, 2H, -OCH-C<u>H_2</u>), δ1.18-0.86 (m for 72H, -CH, -CH_2 and -CH_3); ^{13}C NMR ($CDCl_3$, 400 MHz): δ(ppm) = 161.12, 152.10 (>C=O; carbonate) , 150.22, 150.08, 144.32, 142.16, 140.84, 137.66, 131.18, 130.72, 128.84, 126.91, 126.66, 124.17, 122.32, 121.78, 115.14, 79.08, 68.57, 56.72, 56.27, 50.14, 42.45, 42.34, 39.74, 31.98, 31.95, 31.91, 31.72, 31.60, 31.44, 3128, 31.12, 29.99, 29.95, 29.92, 29.78, 29.60, 29.48, 29.37, 29.29, 29.21, 29.16, 29.06, 28.06, 27.38, 26.64, 25.85, 25.63, 24.38, 23.85, 22.70, 22.44, 22.36, 21.14, 19.45, 18.72, 14.10, 11.84; Elemental analysis: calculated for $C_{62}H_{90}N_2O_4$(%): C, 80.30; H, 9.78; N, 3.02; found: C, 80.57; H, 9.45; N, 3.20.

Compound 7m: Yellow crystalline solid, yield: 86.2%, IR (KBr, ν $_{max}$, cm^{-1}): 3046, 2958, 2921, 2836, 1754, 1604, 1512, 1478, 1238, 844; ^{1}H-NMR ($CDCl_3$, 400 MHz): δ(ppm) = δ6.99-8.20 (m, 12 H, Ar-H), δ5.46 (m, 1H, -C=CH-) δ4.60 (m, 1H -OC<u>H</u>-CH_2), δ4.08 (t, 2H, -OC<u>H_2</u>-CH_2-), δ2.50-2.54 (m, 2H, -OCH-C<u>H_2</u>), δ1.16-0.87 (m for 76H, -CH, -CH_2 and -CH_3); ^{13}C NMR ($CDCl_3$, 400 MHz): δ(ppm) = 161.12, 152.10 (>C=O; carbonate) , 150.24, 150.08, 144.32, 142.18, 140.86, 137.65, 131.17, 130.74, 128.83, 126.94, 126.64, 124.18, 122.34, 121.78, 115.16, 79.08, 68.56, 56.77, 56.28, 50.16, 42.47, 42.36, 39.74, 31.98, 31.96, 31.93, 31.91, 31.90, 31.74, 31.59, 31.44, 31.29, 31.15, 29.99, 29.97, 29.96, 29.95, 29.94, 29.91, 29.74, 29.63, 29.46, 29.36, 29.28, 29.20, 29.12, 29.04, 28.08, 27.39, 26.68, 25.84, 25.62, 24.36, 23.82, 22.72, 22.44, 22.38, 21.12, 19.48, 18.70, 14.11, 11.84; Elemental analysis: calculated for $C_{64}H_{94}N_2O_4$(%): C, 80.45; H, 9.92; N, 2.93; found: C, 80.72; H, 9.70; N, 3.18.

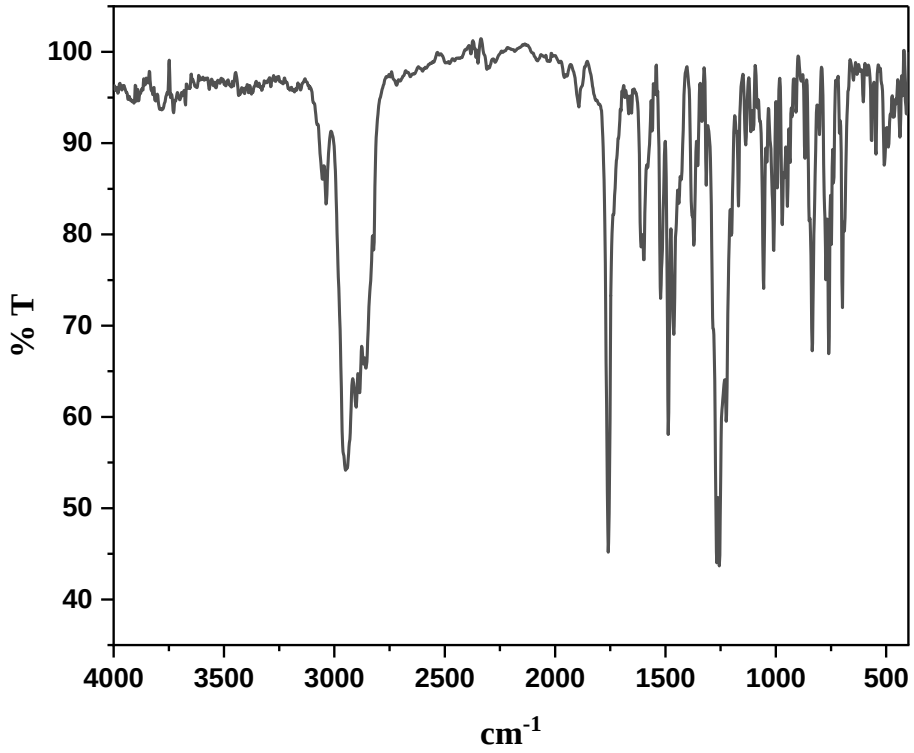

Figure 3.2 (a): FT-IR spectra of **Compound 7a**

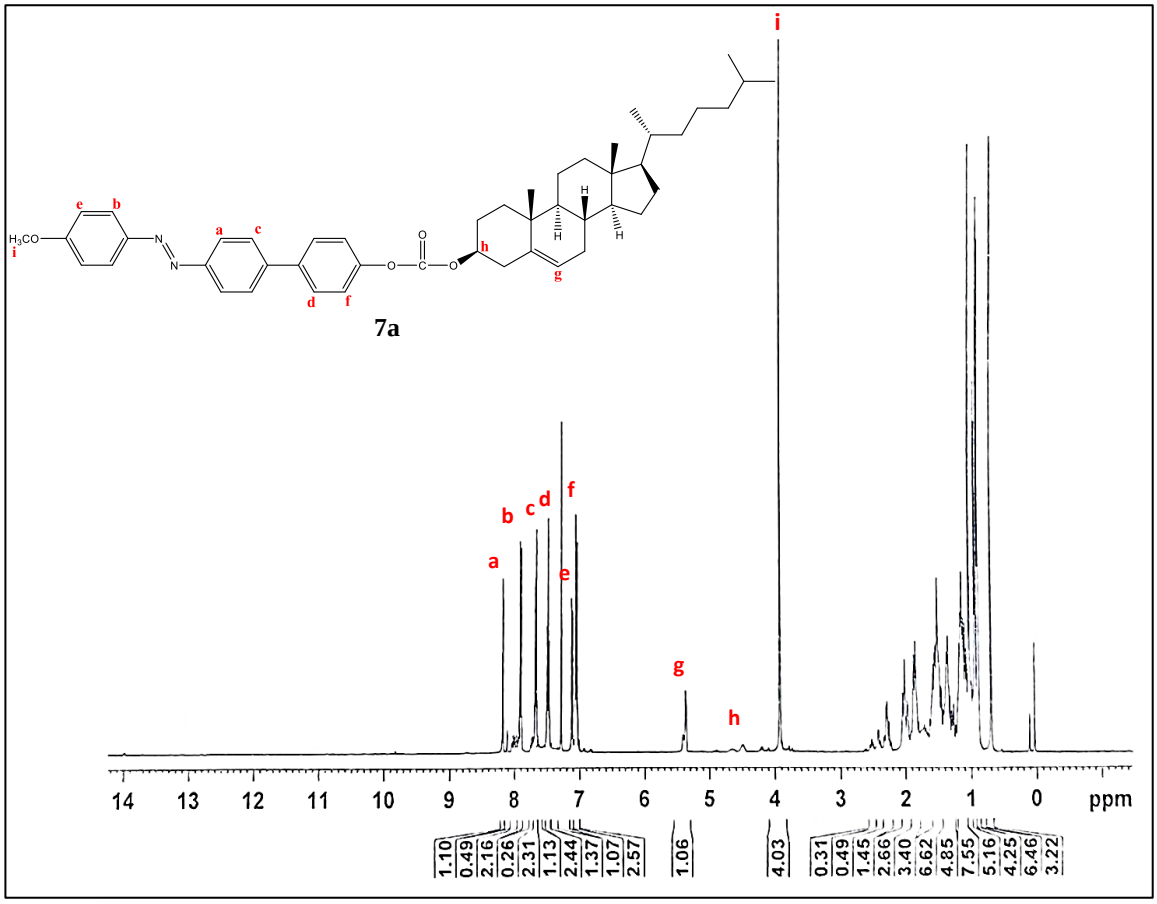

Figure 3.2 (b): ^{1}H-NMR spectra of **Compound 7a**

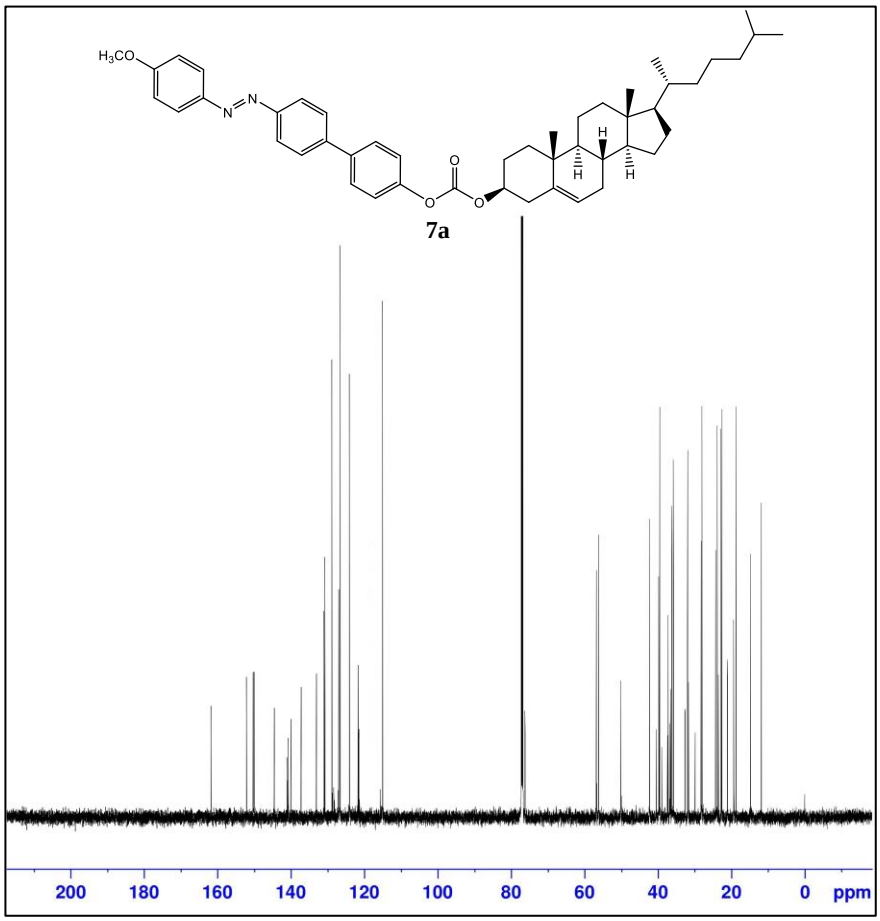

Figure 3.2 (c): ^{13}C-NMR spectra of **Compound 7a**

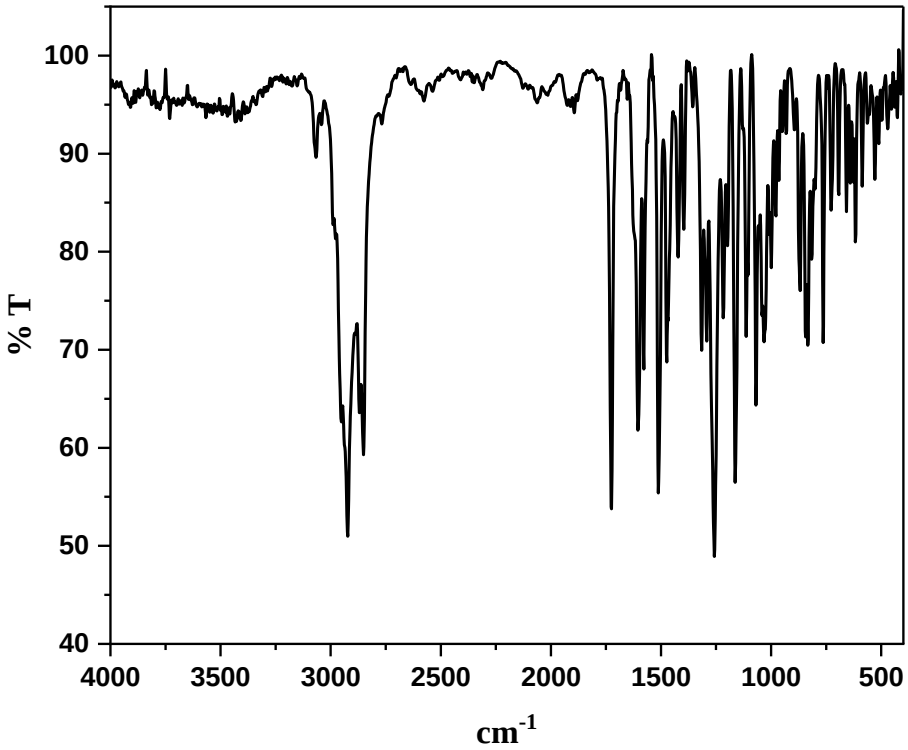

Figure 3.3 (a): FT-IR spectra of **Compound 7i**

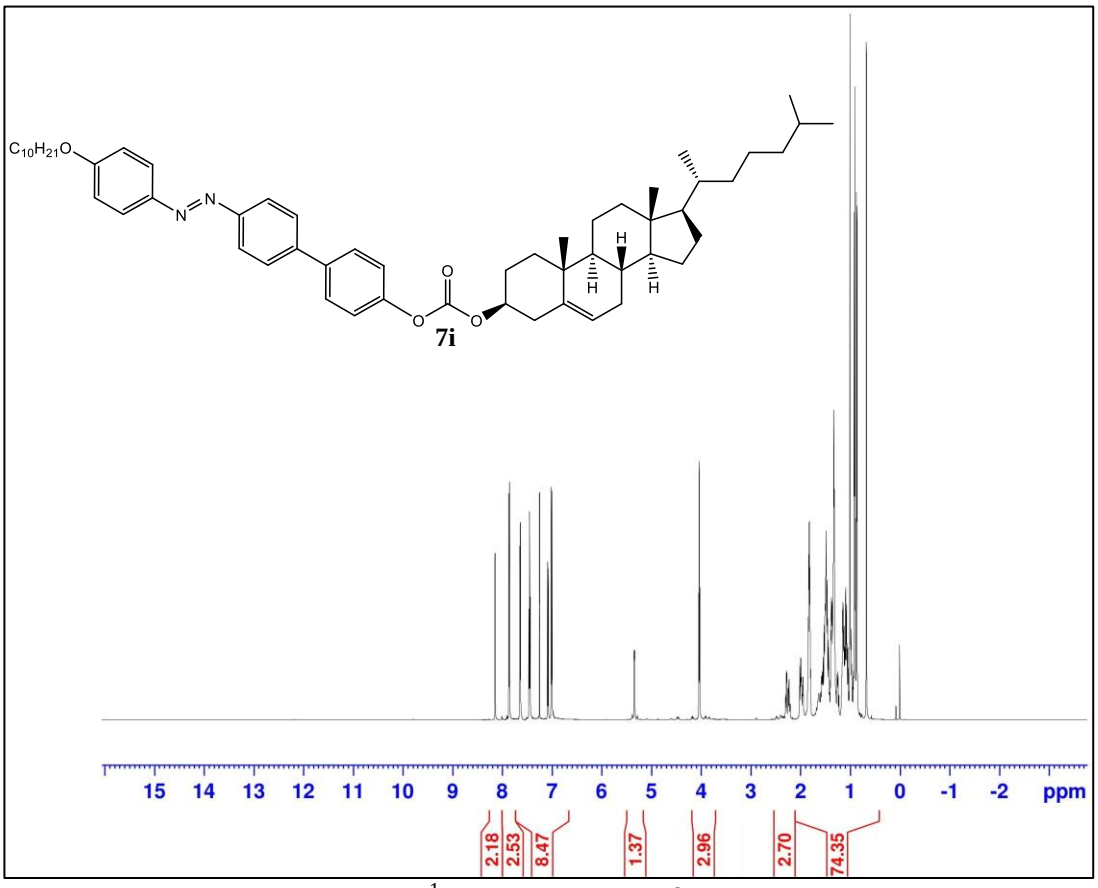

Figure 3.3 (b): ^{1}H-NMR spectra of **Compound 7i**

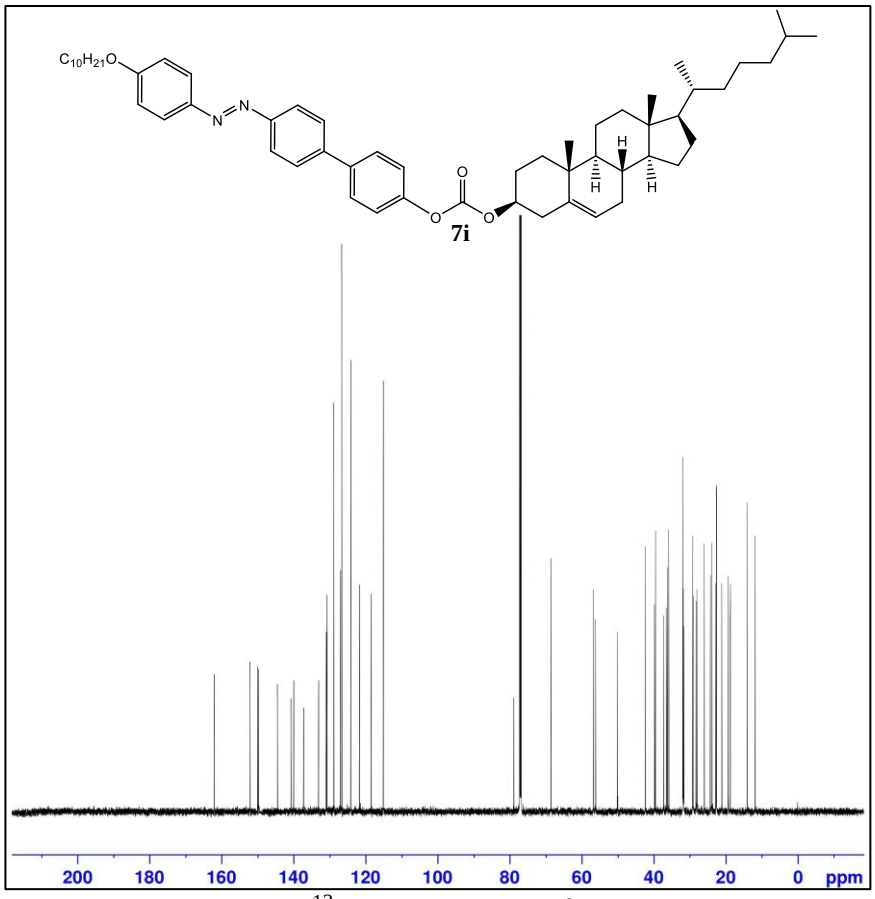

Figure 3.3 (c): ^{13}C-NMR spectra of **Compound 7i**

3.3. Results and discussion

3.3.1. Structural characterization

The final compounds **(7 a-m)** were prepared by condensation of cholesteryl carbonate **(6)** with the appropriate 4′-(4-n-alkoxyphenyl) diazenyl-1,1'-biphenyl-4"-ol **(5 a-m)**. The synthetic route adopted is given in Scheme 3.1. All the compounds in the series exhibit mesomorphism. The lower homologues from methyl to n-hexyl exhibits enantiotropic chiral nematic mesophase. The n-heptyl to n-decyl derivatives of the series show enantiotropic SmA-TGB_A-N*- Isotropic transition. Lastly, the higher homologues from n-dodecyl to n-octadecyl exhibits SmA mesophase in heating as well as cooling cycles. Their DSC thermograms correlate well with the observations from polarizing optical microscopy. Additionally, thermogravimetric analysis indicates that the compounds exhibit thermal stability up to temperatures ranging from 297–338°C.

The FT-IR and NMR spectra, as well as the elemental analyses, are in complete agreement with the structure. In IR spectra, the compound **(7a)** displays prominent bands (ν_{max}, cm^{-1}) at 3037, 2949, 2901, 2854 (CH aliphatic), 1757 (CO carbonate), 1597, 1521 (-C=C-; aromatic), 1487 cm^{-1} (-N=N-; azo). The appearance of peaks at 1757 cm^{-1} and 1487 cm^{-1} confirms the formation of azo carbonate linkages in **7a**.

The proton NMR of the final compound 4'-(4-methoxyphenyl) diazenyl-1,1'-biphenyl-4"-cholesteryl carbonate **(7a)** depicts signals at δ7.01-8.25 (m, 12 H, Ar-H), δ5.46 (m, 1H, olefinic H in cholesterol), δ4.6 (m, 1H, H of cholesterol near carbonate linkage), δ3.91 (s, 3H, $-OCH_3$), δ2.56 (m, 2H, -OCH-$C\underline{H}_2$), δ2.05-0.70 (m for 41H, -CH, $-CH_2$ and $-CH_3$ of cholesterol) ppm, respectively. The ^{13}C NMR spectrum of the compound **(7a)** exhibits prominent signal at δ162.8 (C near methoxy group), δ150.0 (carbonate carbon -O-COO-), and δ129.5-114.6 (carbons of aromatic rings) ppm thereby confirming the formation of the final compound **7a**.

The rest of the members in the series displayed similar IR and NMR (^1H and ^{13}C) spectra, which are outlined in the synthetic part.

3.3.2. Texture analysis

To explore the liquid crystalline properties of the synthesized compounds, they were placed between two untreated glass slides. Optical texture analyses were conducted as the samples underwent heating and cooling cycles using an optical polarizing microscope equipped with a heating stage. Throughout the repeated cycles of heating and cooling, all compounds

exhibited stability. It was observed that all synthesized compounds exhibit mesogenic characteristics.

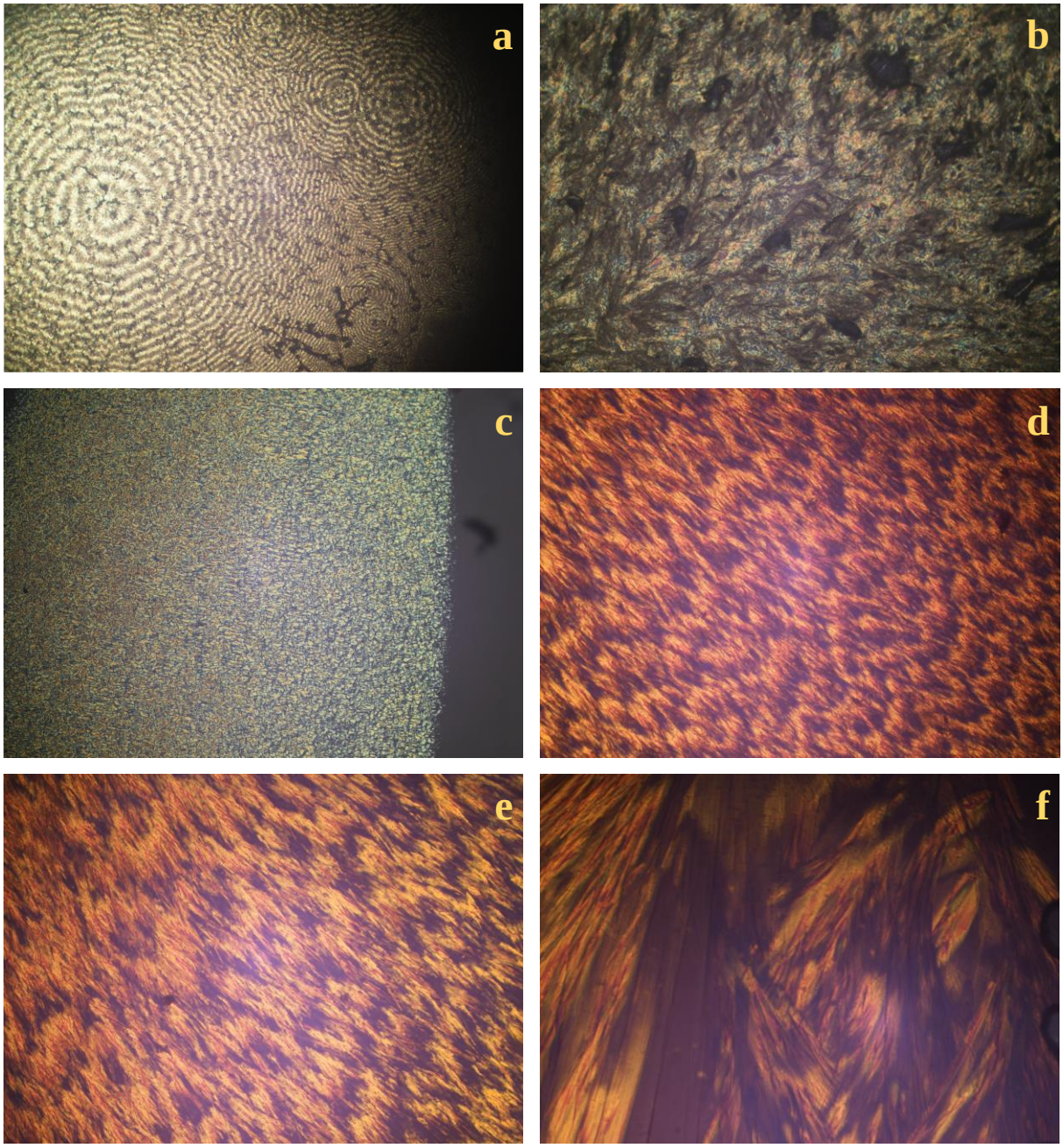

Figure 3.4: Microphotographs of the textures observed under POM for the different LC phases of compounds placed between two untreated glass substrates **(a)** Fingerprint texture of cholesteric or chiral nematic (N*) phase of **1b** at 170°C, **(b)** crystal phase of compound **1b** at 72°C, **(c)** SmA-TGB$_A$-N* phase transition of **7h** at 141°C, **(d)** SmA mesophase of compound **7j** at 130°C, **(e)** SmA mesophase of compound **7m** at 122°C, **(f)** crystal phase upon cooling from SmA mesophase of compound **7m** at 80°C

In the series of compounds, the lower homologues ranging from methyl to n-hexyl **(7a-7f)** display distinct fingerprint textures **(Figure 3.4 (a))** characteristic of the chiral nematic mesophase [31], which persists until reaching the isotropic state. As the compound cooled from the isotropic liquid phase, it displayed fingerprint textures of chiral nematic mesophase until crystallization occurred **(Figure 3.4 (b))**. It falls within the category of thermotropic enantiotropic chiral nematic LCs. The n-heptyl to n-decyl **(7g-7i)** homologues within series show Sm A as well as cholesteric mesophases. The SmA to N* transition proceeds through and intermideated TGB_A phase **(Figure 3.4 (c))**. The pseudo-isotropic SmA texture can be observed, which appears black for all orientations of the sample between crossed polarizers. The frustrated TGB_A phase exhibits a typical filament texture at the SmA-TGB_A transition area and a fan-like texture at slightly higher temperatures [32]. Here, SmA phase is seen as black areas, because here the optic axis is oriented along the direction of light propagation. The higher derivatives of the series **(7j-7m)** exhibits SmA mesophase [16] in both heating and cooling cycles **(Figure 3.4 (d** and **e)). (Figure 3.4 (f))** displays crystal phase upon cooling from SmA mesophase.

Table 3.1: Phase transition temperature of compounds **7a-m** [a, b]

Sample code	n-alkyl chain	Heating Temp °C [ΔH kJ mol^{-1}]	Cooling Temp °C [ΔH kJ mol^{-1}]
7a	**1**	Cr 116.0 [21.35] N* 189.2 [1.29] I	I 188.6 [1.12] N* 70.4 [26.48] Cr
7b	**2**	Cr 122.3 [20.72] N* 187.5 [1.68] I	I 185.8 [1.77] N* 74.3 [19.48] Cr
7c	**3**	Cr 129.7 [24.65] N* 180.4 [1.07] I	I 179.0 [1.50] N* 80.7 [23.25] Cr
7d	**4**	Cr 134.3 [22.57] N* 177.2 [1.35] I	I 176.1 [1.94] N* 77.4 [19.90] Cr
7e	**5**	Cr 137.6 [20.26] N* 170.9 [1.05] I	I 169.2 [1.21] N* 80.6 [28.58] Cr
7f	**6**	Cr 139.1 [27.50] N* 168.3 [1.46] I	I 166.8 [1.37] N* 82.0 [30.63] Cr
7g	**7**	Cr 130.6 [24.45] SmA-TGB_A [c] 144.1 [1.04] N* 162.8 [0.98] I	I 160.3 [1.18] N* 138.0 [1.27] TGB_A-SmA [c] 64.5 [22.87] Cr

7h	**8**	Cr 128.0 [26.83] SmA-TGB_A[c] 143.5 [1.54] N* 160.4 [1.04] I	I 158.8 [1.28] N* 139.6 [1.69] TGB_A-SmA[c] 68.2 [21.76] Cr
7i	**10**	Cr 125.2 [28.60] SmA-TGB_A[c] - 146.5 [1.32] N* 154.2 [1.17] I	I 151.5 [1.08] N* 140.1 [1.44] TGB_A-SmA[c] 63.6 [31.37] Cr
7j	**12**	Cr 126.8 [24.56] SmA 148.6 [3.90] I	I 147.2 [2.73] SmA 85.4 [18.38] Cr
7k	**14**	Cr 126.1 [23.30] SmA 141.7 [3.81] I	I 139.9 [3.81] SmA 88.2 [19.69] Cr
7l	**16**	Cr 122.7 [24.40] SmA 138.0 [4.09] I	I 136.8 [3.98] SmA 90.4 [22.54] Cr
7m	**18**	Cr 120.3 [23.45] SmA 139.2 [5.05] I	I 137.1 [4.94] SmA 82.6 [20.34] Cr

Cr = crystal, SmA = smectic A phase, N* = chiral nematic/ cholesteric phase, TGB_A = twist grain boundary A phase, I = isotropic.

[a]Phase transition temperatures were determined/confirmed by both Polarising optical microscope (POM) and differential scanning calorimetry (DSC) studies: peak temperatures in the DSC thermograms obtained during the first heating and cooling cycles (scanning rate = 5°C min^{-1}) coupled with POM measured temperatures are given; [b]Transition temperatures of some of the compounds were determined with the aid of a POM study as the expected well-resolved thermograms of both heating and cooling cycles could not be obtained; [c]Although TGB_A–SmA/ SmA–TGB_A phase transitions were observed in POM, they were not resolved in DSC traces; hence the enthalpy value represents the combined enthalpy for TGB_A–SmA/ SmA–TGB_A transitions.

3.3.3. Thermal properties

Table 3.1 provides a concise overview of the phase transition temperatures, enthalpy alterations, and mesophase textures observed for the compounds **(7 a–m)**. The thermal properties of all the compounds were assed using Diffrential Scanning Calorimetry (DSC) **(Figure 3.5 (a)** and **(b))** and Thermogravimetric analysis (TGA). The enthalpy and entropy changes observed in DSC help characterize the phase behavior and thermodynamic properties of liquid crystalline compounds. The lower homologue of the series, from methoxy to n-hexyloxy **(7 a-f)** shows two endothermic and two exothermic peaks. In the heating cycle, endotherm with the high ΔH value corresponds to the Cr-N* transition, while low ΔH value signifies the N*-Iso transition, while in cooling cycles the exotherm with low and high ΔH

value corresponds to Iso-N* and N*-Cr transition respectively. The compounds **(7 g-i)** shows three enothermic as well as three exothermic peaks. The peaks in both heating and cooling cycles corresponds to Cr-N*, N*-SmA-TGB_A and SmA-TGB_A-Iso transition. The higher homologues of the series **(7 j-m)**, shows two endotherm corresponding to Cr-SmA with high ΔH value and SmA-Iso transition with low ΔH value, and two extotherm for Iso-SmA and SmA-Cr mesophase transition.

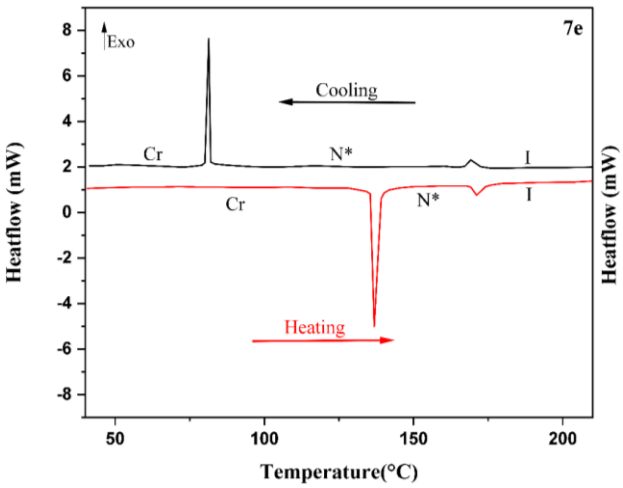

Figure 3.5 (a): DSC thermogram of **7e**

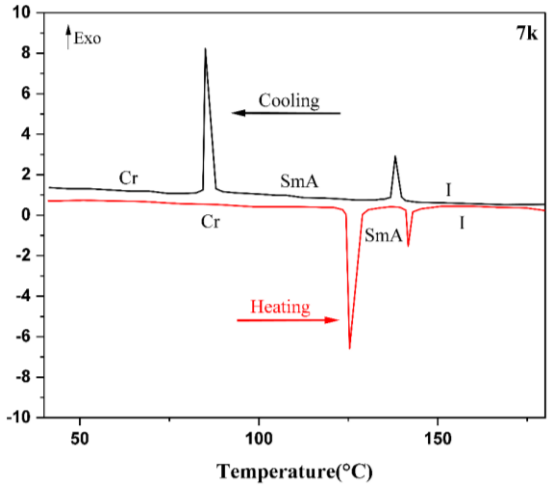

Figure 3.5 (b): DSC thermogram of **7k**

For all the compounds in the series, enthalpy changes are precisely expected throughout the crystal-chiral nematic/smectic A transition. Conversely, the enthalpy changes during the cholesteric-isotropic phase transition are lower than usual. Again, with these types of mesogens, this is to be expected [33]. The Smectic A (SmA) and TGB_A (twist grain boundary A) phases typically do not show an enthalpy change because the transitions between these phases are due to competing intermolecular interactions and strong molecular chirality, as observed in the thermograms of compounds **7 g-i**.

Table 3.2: TGA thermograms decomposition temperatures for compounds **7a,7d,7g,7i,7k** and **7l**

Sample Code	IDT (°C)	50% DT (°C)	FDT (°C)
7a	338	398	683
7d	331	397	724
7g	324	393	704
7i	313	386	709
7k	306	386	658
7m	297	377	647

IDT = initial degradation temperature, 50% DT = 50 % decomposition temperature, FDT = final decomposition temperature

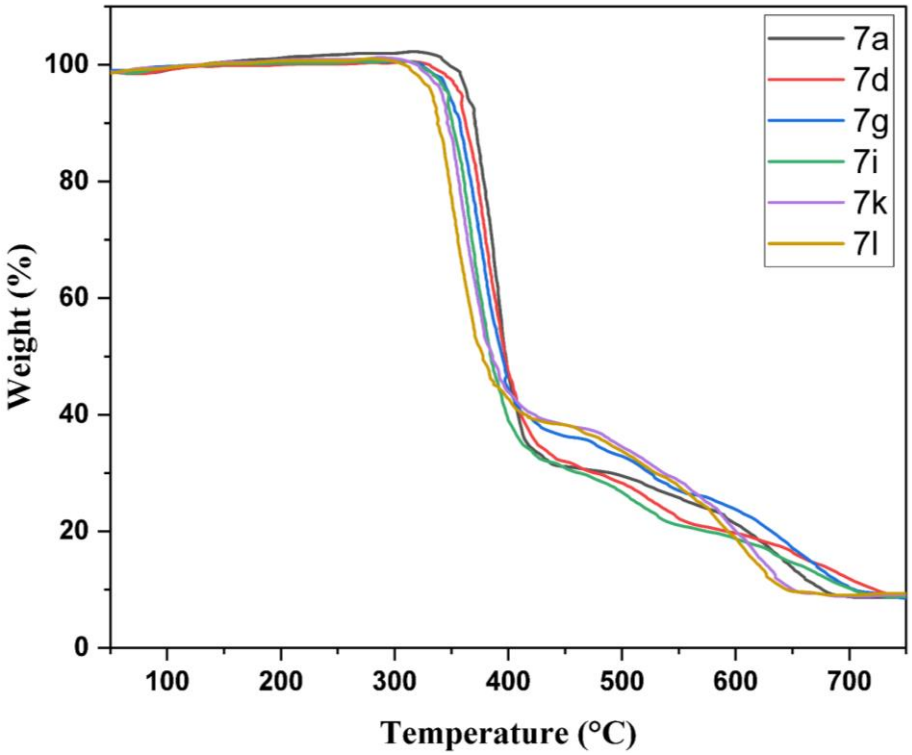

Figure 3.6: TGA profile for some azo-based biphenyl LC

Thermogravimetric analysis (TGA) was employed to assess the thermal stability of compounds **7a**, **7d**, **7g**, **7i**, **7k** and **7l**. The TGA curves, depicted in **Figure 3.6**, illustrate the thermal decomposition behaviour of the azo-carbonate linked liquid crystals. Notably, all compounds exhibited thermal decomposition temperatures surpassing 290°C. The TGA parameters, detailed in **Table 3.2**, encompassed temperatures of initial decomposition, 50% decomposition, and final decomposition, falling within the ranges of 297–338°C, 377–398°C and 647–724°C, respectively. Additionally, the weight loss percentages ranged from 90.24% to 93.87%.

3.3.4. Structure-mesomorphic property relationship

Figure 3.7 illustrates the transition temperature plotted against the number (n) of carbon atoms in the alkoxy chain. The transition curves for Cr-mesophase, SmA-N*, and N*/SmA-Iso were derived from this graph. The N*/SmA to isotropic transition temperatures show a sharp decrease, while the SmA to N* transition displays an increase as the terminal chain length increases. Initially, the curve for the Cr to first mesophase rises to a peak with the heyloxy derivative, followed by a decline that remains nearly parallel to the N*/SmA to isotropic curve for higher homologues. In Series I compounds, there is a inclination for the

chol-iso phase transition to decrease with increasing terminal chain length, and the appearance of the smectic phase in middle member homologues is also a typical trend. Such a specific pattern is anticipated in this system [34,35]. Lower homologues, with minimal parting of aromatic part and higher terminal organisations, exhibit entirely nematogenic behaviour. However, as we move up the series, lateral cohesive forces increase, leading to a layered molecular structure before entering the nematic phase. With longer terminal chain lengths, the relatively weak end group inter-molecular interactions are insufficient to uphold equivalent molecular alignment, favouring smectogenic properties over nematic phase stability.

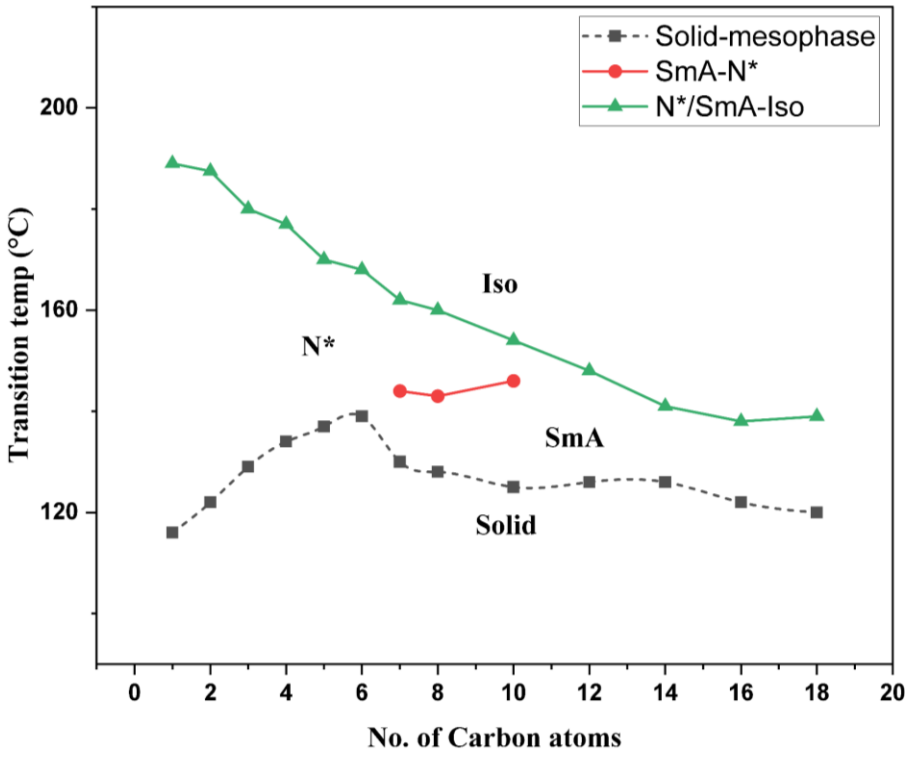

Figure 3.7: Plot of transition temperatures (°C) versus number of carbon atoms in the alkoxy chain for compounds **7 a-m**

The liquid crystalline properties of organic compounds are elaborately linked to their molecular structure, influencing their thermal stability. By analyzing the molecular composition, a correlation emerges between their mesogenic properties and thermal stability, as indicated by parameters like SmA/N* - Iso (clearing temperatures) and SmA - N* (stability of different phases). **Table 3.3** offers a comparative overview of thermal stabilities across different LC series.

Comparison of the molecular structure of the current **Series I** with previously reported series.:

(1) 4'-(4-alkoxyphenyl) diazenyl-1,1'-biphenyl-4"-cholesteryl carbonate; **Series I**

(2) “4'-[(4-n-alkoxyphenyl) diazenyl]4-butoxy phenyl biphenyl carboxylate”; **Series A** [30]

(3) “Cholesteryl 4'-alkyloxybiphenyl-4-carboxylates”; **Series B** [36]

The geometry of the compounds are shown in **Figure 3.8**.

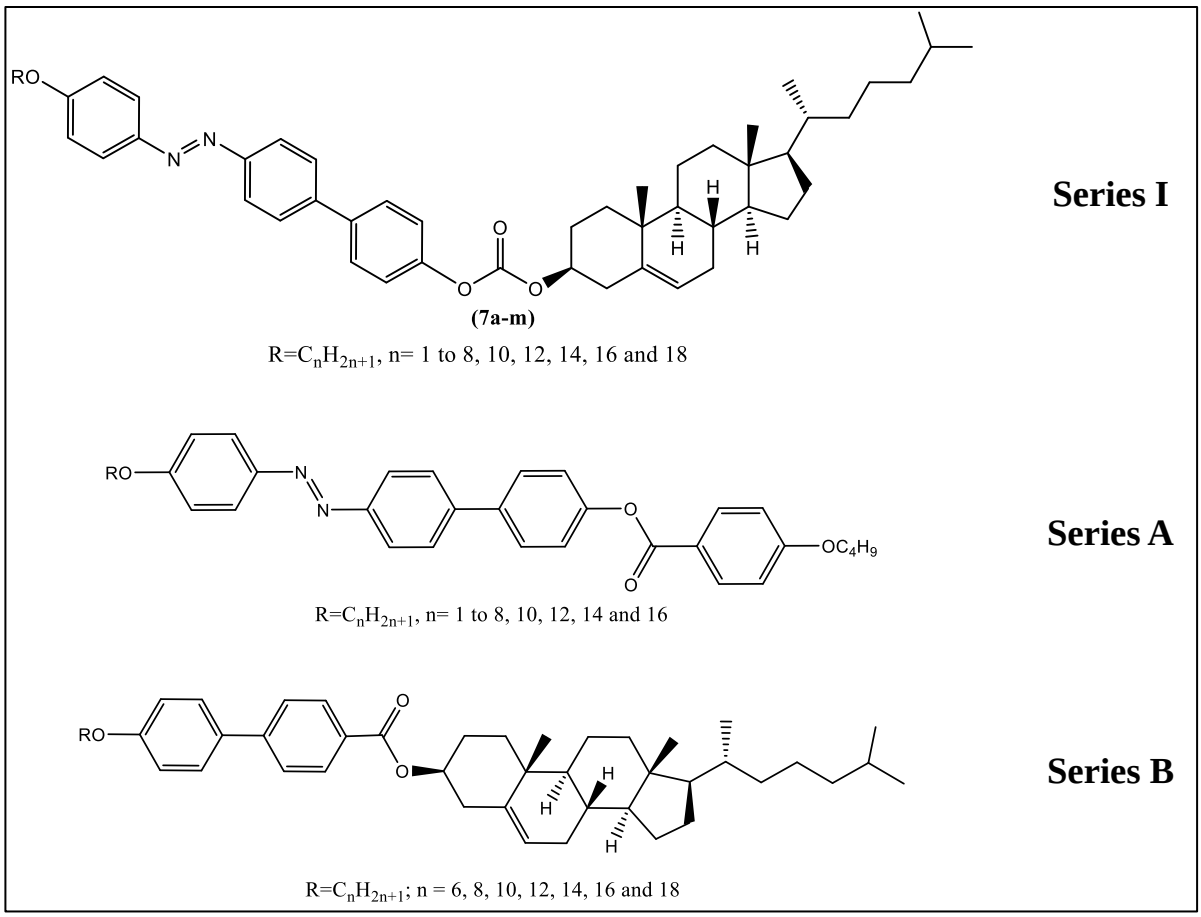

Figure 3.8: The geometric comparison of **Series I, A** and **B**

In Series I, 4′-(4-n-alkoxyphenyl) diazenyl-1,1'-biphenyl-4"-ol is linked to the cholesteryl chloroformate forming carbonate linkage, whereas in Series A 4′-(4-n-alkoxyphenyl) diazenyl-1,1'-biphenyl-4"-ol is linked to 4-n-alkoxy benzoyl chloride forming ester linkage. The higher SmA/N* - Iso thermal stability of Series I can be attributed to the cholesterol moiety as compared to the long alkyl chain in Series A. Cholesterol's rigid, planar structure and multiple rings enable close packing in the solid state, resulting in stronger intermolecular forces and a higher melting point. In contrast, alkyl chain derivatives have simpler, linear structures with weaker intermolecular forces and lower melting points. Additionally, the presence of a cholesterol moiety in Series I enhances the stability of the nematic phase in the SmA - N* transition by introducing chirality and forming a helical structure, aiding in maintaining molecular alignment and reducing thermal fluctuations. Series I exhibit a chiral nematic (cholesteric) mesophase due to chirality, while Series A remains purely smectogenic because of the biphenyl ring, leading to lamellar bunch formation.

In Series B, the cholesterol moiety is linked to the 4′-(4-n-alkyloxyphenyl) benzoic acids, forming an ester linkage. This molecule lacks the azo linkage as present in Series I. The SmA/N* - Iso transition temperature of Series I is extremely low as compared to the Series B. The presence of the azo linkage can introduce flexibility into the molecular structure, especially if it is located between two flexible aromatic rings. Increased molecular flexibility can disrupt the packing of molecules in the solid state, leading to weaker intermolecular interactions and a lower melting point.

Table 3.3: Average thermal stabilities (°C) of Series I, A and B compounds.

Series	**I**	**A**	**B**
SmA/N* - Iso ($C_{6,8,10,12,14,16}$)	151.8	106.8	262.6
SmA - N*	144.7 ($C_{7,8,10}$)	-	213.7 ($C_{6,8,10}$)

3.3.5. Radical-scavenging activity of mesogens

All the synthesized mesogens were tested for their radical scavenging activity (anti-oxidant activity) using the DPPH free radical assay and method described in the literature [37]. 0.01 mg/mL (0.001% (w/v)) solution of DPPH in methanol was prepared and mixed with an equal amount of standard antioxidant and synthesized 1,3,4-oxadiazoles dissolved in methanol. Stock solutions of synthesized compounds (1 mg/mL) was diluted to a final concentration of 50, 100, and 200 µg/mL in DMSO. The absorbance was recorded at 517 nm using a Shimadzu UV-1800 spectrophotometer from Japan after a 30-minute incubation in darkness. The DPPH radical scavenging activity of synthesized compounds has been compared to the well-known reference antioxidant, ascorbic acid. DPPH radical scavenging activity was determined as:

$$\text{“\% Inhibition} = [(A_{control} - A_{sample}) / A_{control}] \times 100\text{”}$$

where $A_{control}$ = absorbance of the control, As_{ample} = absorbance of the test compounds.

Results are represented as a percentage of inhibition and an IC_{50} value, which represents the effective concentration needed to scavenge 50% of the original DPPH. It was compared to the referent ascorbic acid.

The findings from **Table 3.4** reveal that all compounds exhibit moderate to good radical scavenging activity. Particularly noteworthy is that the lower homologues demonstrate superior activity compared to their higher homologue counterparts. Compound **7a** displayed the highest activity, with an IC_{50} value of 69.09 µg/ml, whereas compound **7l** exhibited the lowest activity,

with an IC_{50} value of 140.85 µg/ml among all compounds tested. The enhanced activity observed in the lower homologues is likely attributed to their smaller molecular size and greater solubility.

Table 3.4: Radical-scavenging activity of mesogens: % inhibition and IC_{50} values of the DPPH free radical scavenging assay

Sample code	% Inhibition[a]			IC 50(µg/ml)
	50 µg/ml	100µg/ml	200µg/ml	
7a	41.87 ± 0.73	62.39 ± 0.10	87.46 ± 0.30	69.09
7b	43.05 ± 0.91	58.44 ± 0.29	83.88 ± 0.80	73
7c	39.36 ± 0.42	60.61 ± 0.76	72.03 ± 0.21	80.54
7d	39.84 ± 0.81	58.89 ± 0.62	74.01 ± 0.58	81.69
7e	38.60 ± 0.58	60.80 ± 0.89	77.69 ± 0.12	80.18
7f	40.14 ± 0.13	60.32 ± 0.72	72.67 ± 0.10	78.79
7g	36.70 ± 0.87	59.08 ± 0.93	70.55 ± 0.36	90.72
7h	36.17 ± 0.92	55.03 ± 0.40	70.06 ± 0.09	99.23
7i	34.74 ± 0.69	51.09 ± 0.42	68.02 ± 0.58	110.65
7j	30.01 ± 0.42	50.27 ± 0.35	69.43 ± 0.14	117.06
7k	32.41 ± 0.84	48.86 ± 0.46	65.84 ± 0.40	121.13
7l	30.67 ± 0.86	46.34 ± 0.70	59.60 ± 0.16	140.85
7m	30.70 ± 0.79	43.50 ± 0.65	53.40 ± 0.47	140.84
STD[b]	49.64 ± 0.03	66.13 ± 0.03	92.78 ± 0.37	47.69
Blank[c]	-	-	-	-

[a] Values represent the mean ± standard error mean (SEM) of three experiments.

[b] Ascorbic acid used as standard

[c] No inhibition

3.3.6. Photoisomerization behaviour

The photoisomerization behaviour of azobenzene is extensively studied and widely applied. Upon light absorption, azobenzene undergoes photoexcitation, generating a highly reactive excited state. In this state, rapid isomerization occurs from the stable *trans* configuration, where the N=N bond is linear, to the less stable *cis* configuration, where the N=N bond is bent. The *cis*-azobenzene isomer is typically less stable than the *trans*-azobenzene isomer and can thermally relax back to the *trans* configuration. However, the rate of thermal

relaxation is often considerably slower than that of photoisomerization, allowing the *cis* isomer to persist for prolonged periods, subject to environmental factors [38–40].

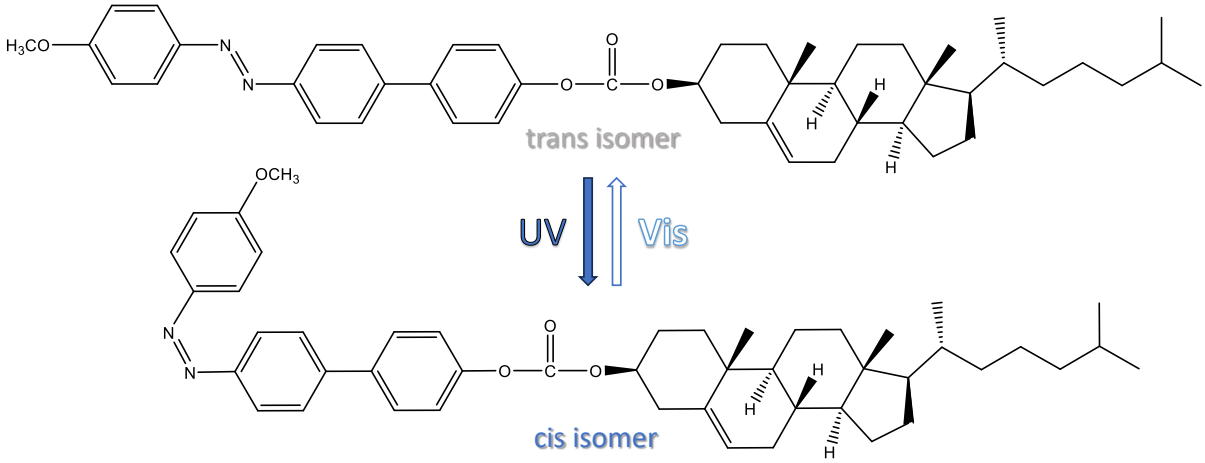

Figure 3.9: *cis-trans* isomerism in azo-based biphenyl liquid crystal

The azobenzene moiety of compound **7a** in its *trans* configuration exhibits a prominent absorption band around 320 nm, attributed to the π-π* transition, along with a weaker absorption band in the visible region around 440 nm, attributed to the n-π* transition. Generally, the *trans*-form is more stable compared to the *cis*-form, although both isomers can interconvert under light irradiation. Upon exposure to UV light, the *trans-cis* transition results in a decrease in absorption around 320 nm and an increase around 440 nm, whereas the reverse *trans-cis* transition under visible light leads to the opposite absorption changes. In the case of compound **7a**, irradiation with 365 nm UV light in its $CHCl_3$ solution (1 x 10^{-5} M) achieves complete *trans-cis* transition within 120s, as depicted in **Figure 3.10 (a)**. Conversely, the reverse *trans-cis* transition process is accomplished within 240s under visible light, as illustrated in **Figure 3.10 (b)**.

The photoisomerization of azobenzene liquid crystals can induce substantial changes in molecular alignment, structure and optical characteristics. When exposed to light, *cis*-isomerization can disrupt the long-range organization of the liquid crystal phase, resulting in shifts in optical properties like anisotropy and birefringence. Furthermore, these changes in molecular orientation offer opportunities for dynamic manipulation of optical features, including modulation of light, switching polarization, and storing optical information.

Due to their unique molecular structure and mesophase properties, azobenzene liquid crystals can be precisely designed for specific photoresponsive behaviours, allowing researchers to tailor them for optoelectronic and photonic applications.

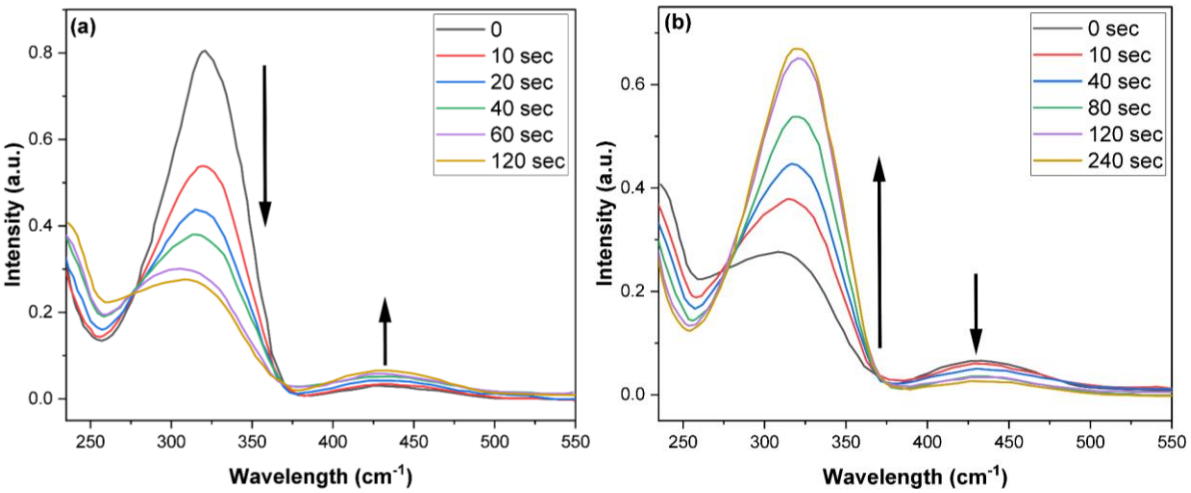

Figure 3.10: Time dependent UV spectra of **7a** in $CHCl_3$ (1 x 10^{-5} M) **(a)** *trans*-to-*cis* isomerization under irradiation with 365 n UV light followed by **(b)** *cis*-to-*trans* isomerization under irradiation with visible light

3.3.7. DFT studies

3.3.7.1. Optimized Molecular Structures and HOMO-LUMO energies

The molecular conformation, molecular orbitals and electrostatic potential of azo-based biphenyl liquid crystals were investigated using DFT analysis. Gaussian 09, version A.02 was used for geometry optimizations and DFT calculations, utilizing the 6-31G (d, p) basis set and the B3LYP hybrid functional [41]. The lack of any imaginary frequency indicates that the optimized structure is in a stable energy state **(Figure 3.11)**. The optimized molecular structure of the compounds is shown in **Figure 3.11**. The optimum energies for certain derivatives are listed in **Table 3.5** and **Figure 3.12** illustrates the relationship between the energy minima in Hartree units and the number of C atoms in the terminal chain of synthesized molecules. The graph shows that the energy minima drop with increasing terminal chain carbon atom atoms, indicating increased molecule stability. This implies that longer chains could result in more conformations that are energetically beneficial, perhaps as a result of the molecule's enhanced flexibility and conformational freedom.

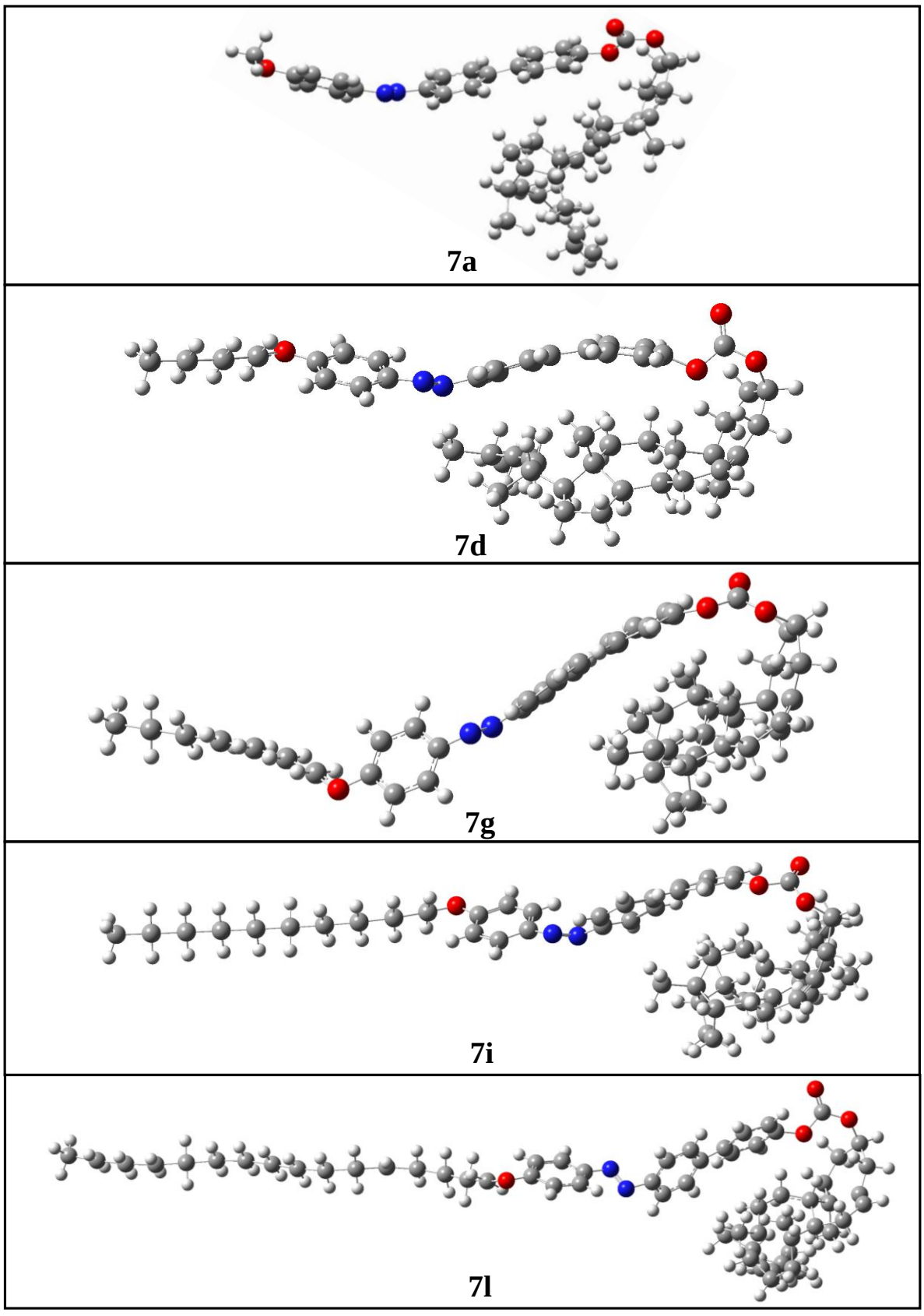

Figure 3.11: Optimized molecular structures of azo-based biphenyl liquid crystals

Table 3.5: Optimized energy (in hartree)

Sample	Energy Minima (Hartree)
7a	-2235.908
7d	-2353.110
7g	-2470.435
7i	-2587.707
7l	-2822.305

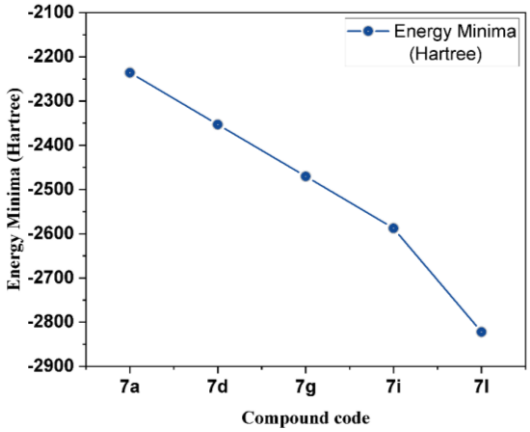

Figure 3.12: Dependence of the terminal alkoxy chain on the energy minima

When assessing a compound's stability, reactivity and light absorption properties, the LUMO and the HOMO are critical factors to consider. Increased stability and lower reactivity are shown by a greater energy difference between the HOMO and LUMO, as the chemical becomes less susceptible to electron donation or acceptance. The electron acceptor is the LUMO, while the electron donor is the HOMO. **Table 3.6** provides the computed energies of the frontier molecular orbitals, including the azo-based biphenyl liquid crystal molecules' HOMO-LUMO energy gap. Furthermore, 3D iso-surface maps of these orbitals for the compounds are shown in **Figure 3.13 (a-c)**.

Table 3.6: Calculated molecular properties of the azo-based biphenyl LC using DFT

Sample	E_{HOMO} (eV)	E_{LUMO} (eV)	ΔE (eV)	η Global hardness	$\delta = 1/\eta$ Global softness	μ_{el} (eV)	ω Electrophilicity index
7a	-4.2784	-2.2931	1.98	0.99	1.00	-3.28	5.43
7d	-4.1965	-2.3682	1.82	0.91	1.09	-3.28	5.89
7g	-3.2185	-2.3175	0.90	0.45	2.21	-2.76	8.50
7i	-3.0327	-2.3654	0.66	0.33	2.99	-2.69	10.91
7l	-2.5641	-2.2871	0.27	0.13	7.22	-2.42	21.24

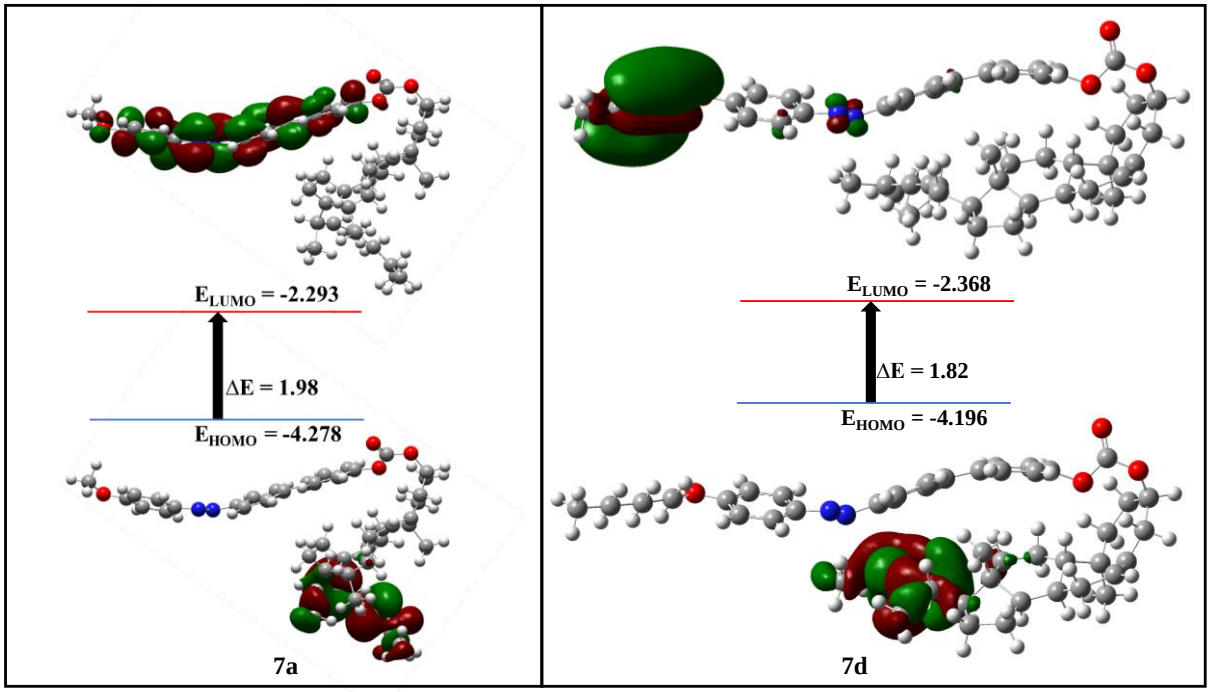

Figure 3.13 (a): FMO contours of structures **7a** and **7d**

The electron density of the orbitals in the HOMO in all the compounds in compounds **7a** and **7d** was mainly concentrated over the iso-octyl side chain of the cholesterol moiety whereas in compounds **7g, 7i** and **7l** it was mainly focused over the alkoxy terminal chains.

Also, the electron density of the orbitals in the LUMO for compound **7a** was observed mainly over the biphenyl ring, azo linkage, phenyl ring and methoxy terminal group. For compounds **7d, 7d** and **7i** it was mainly concentrated over alkoxy side chains, whereas for compound **7l** it was concentrated over the azo linkage, phenyl ring and the alkoxy chain. The energy gap (ΔE) for synthesized compounds were found to be in the range of 1.98 – 0.27 with decreasing trend for increased methylene units. This implies that the lower homologues in the series exhibit greater stability and lower reactivity, while increasing the terminal chains enhances the likelihood of the molecule engaging in electronic transitions and chemical reactions. This suggests heightened reactivity of the molecule, potentially leading to improved electrical conductivity or fluorescence characteristics.

Table 3.6 presents the frontier Molecular Orbital (MO) energy levels and various reactivity parameters for optimized molecular structures [42], providing significant insights into the chemical reactivity and stability of the compounds. The compounds displayed chemical potentials ranging from -2.42 to -3.28 eV and hardness values ranging from 0.13 to 0.99 eV, with the lowest observed for compound **7l**. Compound **7l** exhibits higher reactivity compared to others in the series, indicating its softer nature. Furthermore, a trend of increasing

electrophilicity is noted in the sequence: **7a** < **7d** < **7g** < **7i** < **7l**, suggesting a decrease in electron density or an increase in electron-withdrawing characteristics among the mesogens. Consequently, **7l** displays enhanced reactivity towards electrophiles.

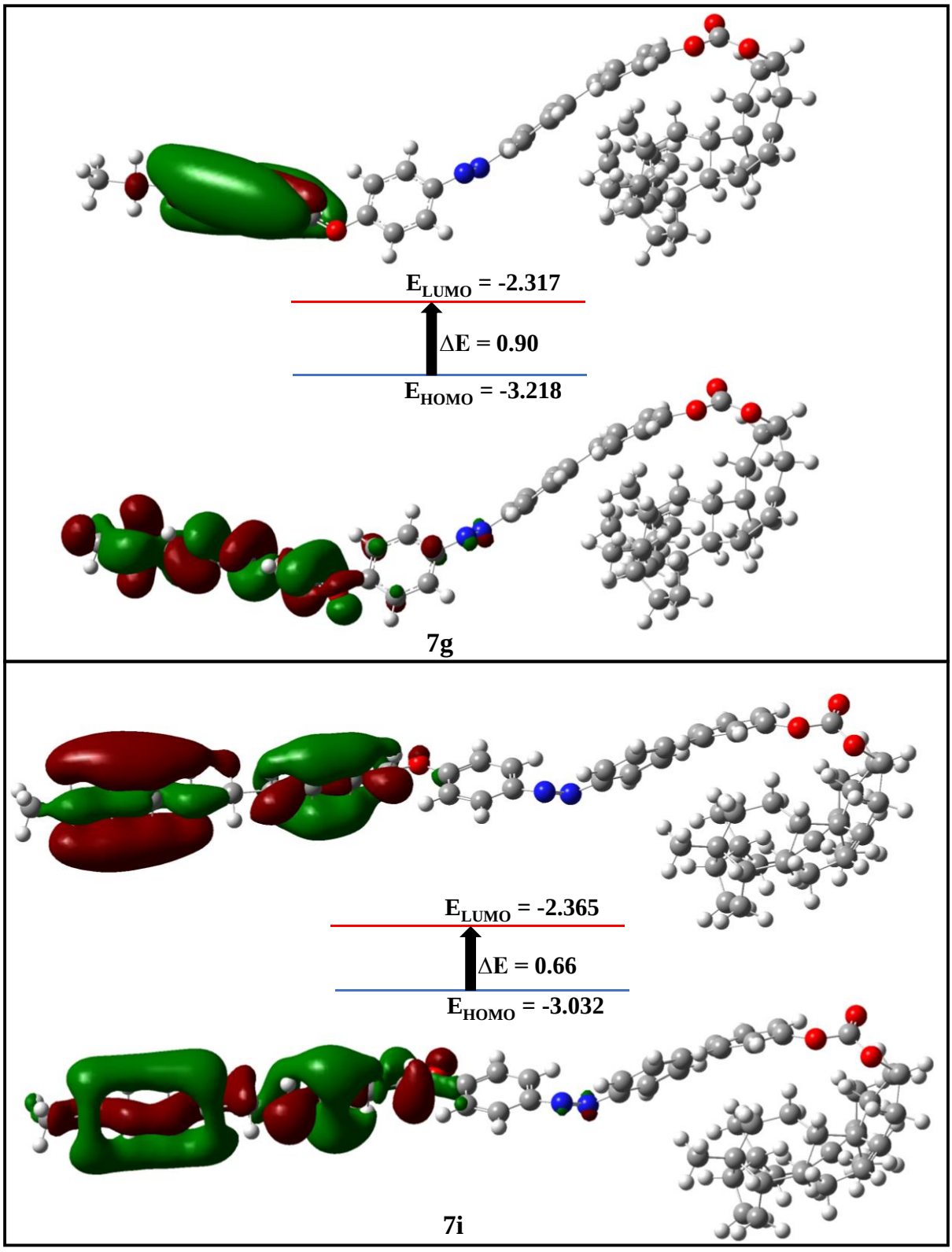

Figure 3.13 (b): FMO contours of structures **7g** and **7i**

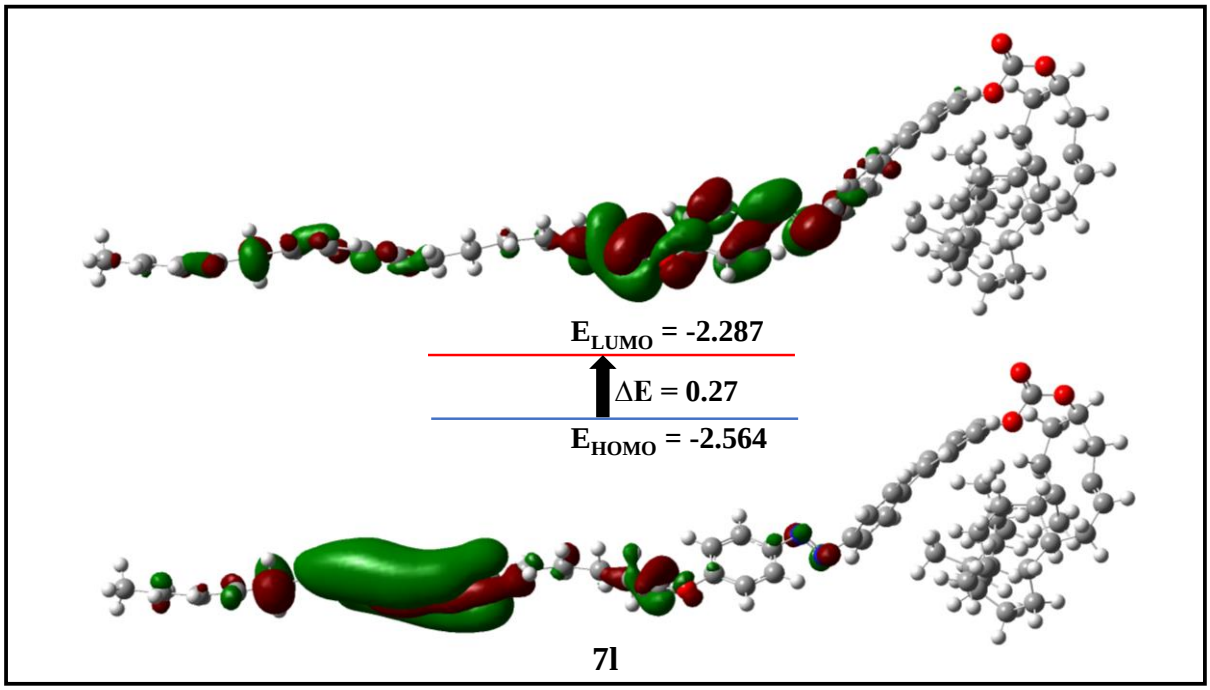

Figure 3.13 (c): FMO contours of structures **7l**

Table 3.7: Dipole moment for azo-biphenyl LC derivatives

Sample	μ_x	μ_y	μ_z	Dipole Moment μ_{dip} (Debye)
7a	2.3667	1.3619	0.1466	2.7345
7d	7.6635	0.3163	2.1207	7.9578
7g	6.3007	1.4548	-1.2509	6.5863
7i	10.3715	-0.7952	1.6457	10.5313
7l	-6.8294	1.7248	-2.0569	7.3380

Dipole moments have been computationally determined for the selected compounds along three Cartesian axes **(Table 3.7)**. The elevated dipole moments serve as indicators of the mesogenic characteristics of these compounds. Differences in molecular polarity among the samples are reflected in their varying dipole moments. Compounds with heightened dipole moments, such as **7i** and **7l**, are anticipated to possess more polarized molecules, while those with lower dipole moments, like **7a** are relatively less polar. These discrepancies in dipole moments play a crucial role in dictating the liquid crystal behaviour, influencing aspects such as phase transitions and optical properties. Elevated dipole moments may potentially amplify electro-optical responses or alter phase transition temperatures.

3.3.7.2. Molecular electrostatic potentials (MEP)

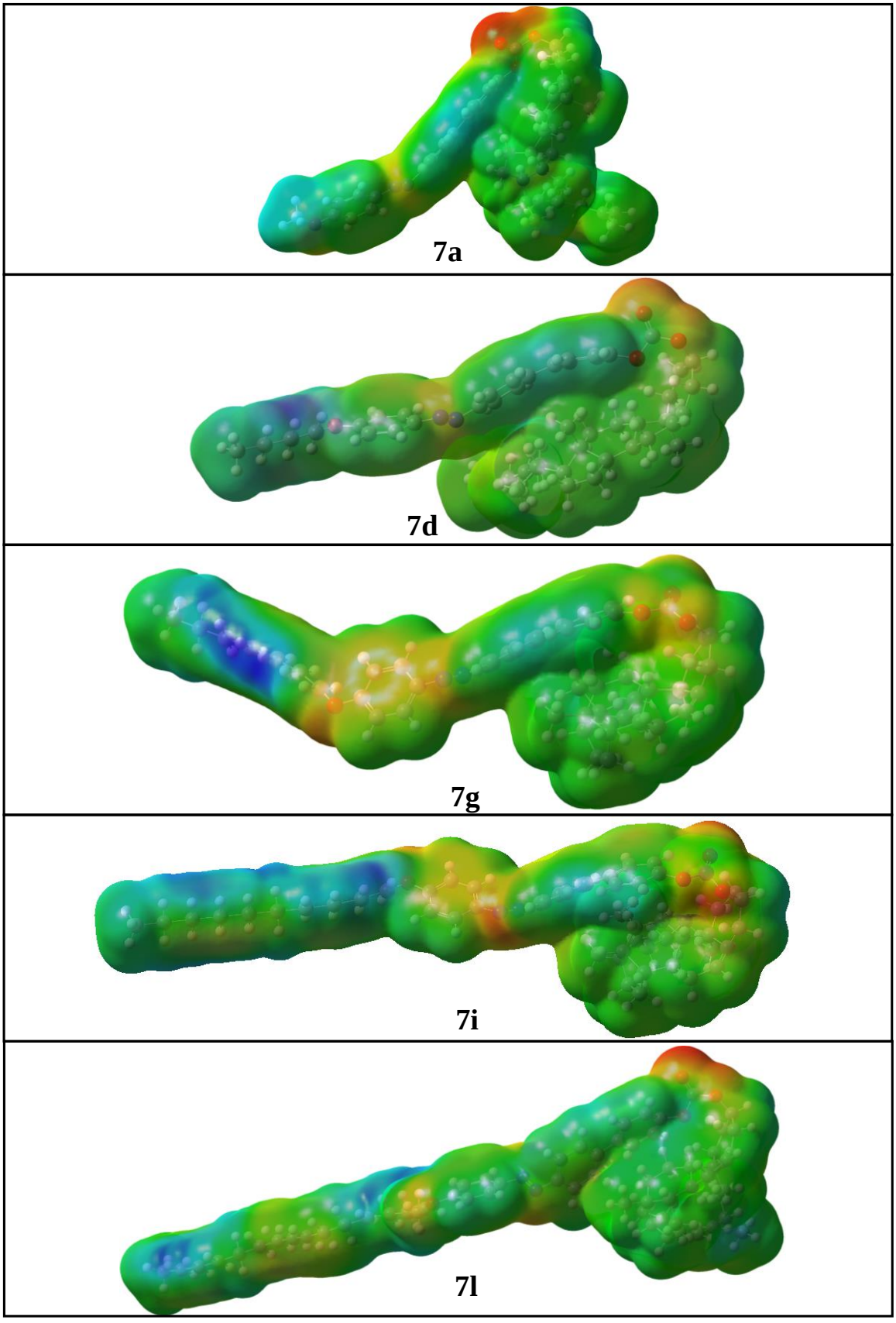

Figure 3.14: Molecular electrostatic potentials (MEP) for selected compounds

In the domain of liquid crystal research, Molecular Electrostatic Potential (MEP) analysis is indispensable for elucidating the behavior and intrinsic properties of liquid crystal molecules. This analytical technique offers a detailed understanding of the electric charge distribution within molecules, which is essential for predicting their interactions, alignment tendencies, and overall stability within liquid crystalline phases. MEP analysis enables researchers to pinpoint regions of high and low electron density, which significantly affect how these molecules respond to external electric fields and their capability to form organized, stable structures. This information is vital for advancing the design and application of liquid crystal materials in various technological fields.

Figure 3.14 illustrates the molecular electrostatic potential map, offering valuable insights into intermolecular interactions. In this visualization, the interaction between electron-rich areas (shown in red) and electron-deficient areas (shown in blue) highlights intermolecular interactions. The red regions, which indicate electron abundance, are mainly concentrated around the carbonate group and azo linkage, marking negatively charged atomic sites. On the other hand, the blue regions signify electron-deficient areas, with the lowest negative charge found at the biphenyl moiety and terminal alkoxy chains.

3.4. Conclusion

This study presents a systematic protocol for synthesizing homologous cholesterol based azo-biphenyl liquid crystalline compounds with various alkoxy side chains. All of the synthesized compounds are mesogenic in nature. The methyl to n-hexyl homologues show enantiotropic cholesteric mesophases. The n-heptyl to n-decyl compounds display SmA to isotropic transition with an interceding TGB_A phase. The higher homologues, from n-dodecyl to n-octadecyl show enantiotropic SmA mesophase. In the graph illustrating transition temperatures versus the number of C-atoms in terminal chain, the N*/SmA to isotropic transition temperatures show a sharp decrease, while the SmA to N* transition displays an increase as the terminal methylene units increases. Initially, the curve for the Cr to first mesophase rises to a peak with the hexyloxy derivative, followed by a decline that remains nearly parallel to the N*/SmA to isotropic curve for higher homologues. All the compounds show good thermal stability ranging from 297 to 338 °C. All the compounds show moderate anti-oxidant activity. Additionally, compounds exhibited photoisomerization behaviour in dilute solutions. Theoretical chemical reactivity studies were performed using Density Functional Theory calculations, emphasizing the analysis of Frontier Molecular Orbitals and Molecular Electrostatic Potential mapping. These calculations aimed to identify energy gaps

and regions of low and high electron density. The photoswitching properties makes them a strong candidate for electronic and optical device applications. This capability can be harnessed in various advanced technologies, such as light-responsive displays, data storage devices and smart windows.

3.5. References

[1] Yelamaggad CV, Shanker G, Hiremath US, et al. Cholesterol-based nonsymmetric liquid crystal dimers: an overview. J Mater Chem. 2008;**18**:2927–2949.

[2] Mitov M. Cholesteric Liquid Crystals with a Broad Light Reflection Band. Advanced Materials. 2012;**24**:6260–6276.

[3] Oh S-W, Baek J-M, Kim S-H, et al. Optical and electrical switching of cholesteric liquid crystals containing azo dye. RSC Adv. 2017;**7**:19497–19501.

[4] Yang S, Li J, Wei J. A real-time temperature responsive material based on partial inverse opal photonic crystals and cholesteric liquid crystals. Optical Materials. 2022;**124**:111992.

[5] Albuquerque HMT, Santos CMM, Silva AMS. Cholesterol-Based Compounds: Recent Advances in Synthesis and Applications. Molecules. 2019;**24:**116.

[6] W. Goodby J. Chirality in liquid crystals. Journal of Materials Chemistry. 1991;**1**:307–318.

[7] Donaldson T, Henderson PA, Achard MF, et al. Non-symmetric chiral liquid crystal trimers. Liquid Crystals. 2011;**38**:1331–1339.

[8] Yelamaggad CV, Bonde NL, Achalkumar AS, et al. Frustrated Liquid Crystals: Synthesis and Mesomorphic Behavior of Unsymmetrical Dimers Possessing Chiral and Fluorescent Entities. Chem Mater. 2007;**19**:2463–2472.

[9] Paterson DA, Walker R, Abberley JP, et al. Azobenzene-based liquid crystal dimers and the twist-bend nematic phase. Liquid Crystals. 2017;**44**:2060–2078.

[10] Paterson DA, Xiang J, Singh G, et al. Reversible Isothermal Twist–Bend Nematic–Nematic Phase Transition Driven by the Photoisomerization of an Azobenzene-Based Nonsymmetric Liquid Crystal Dimer. J Am Chem Soc. 2016;**138**:5283–5289.

[11] He W-L, Li M, Liu S-Q, et al. Synthesis of chiral azobenzene derivatives and the performance in photochemical control of blue phase liquid crystal. Liquid Crystals. 2018;**45**:370–380.

[12] He W-L, Gu H, Zhao P, et al. Synthesis and mesophase behaviour of branched azobenzene-based supramolecular hydrogen-bonded liquid crystals. Liquid Crystals. 2017;**44**:593–602.

[13] Tan X, Li Z, Xia M, et al. Reversible photoresponsive chiral liquid crystal and multistimuli responsive organogels based on a cholesterol-azobenzene dimesogen. RSC Adv. 2016;**6**:20021–20026.

[14] George M, Mallia VA, Antharjanam PKS, et al. Synthesis and Photoswitching Properties of Some Cholesterol Based Liquid Crystals. Molecular Crystals and Liquid Crystals Science and Technology Section A Molecular Crystals and Liquid Crystals. 2000;**350**:125–139.

[15] Gupta M, Pal V, Pal SK. Photo-responsive liquid crystals derived from azobenzene centered cholesterol-based tetramers. New J Chem. 2018;**42**:8765–8772.

[16] Mali H, Sharma VS, Rathod SL, et al. Synthesis, characterization and photophysical study of cholesterol functionalized azo-based room temperature liquid crystals. Journal of Molecular Structure. 2023;**1289**:135776.

[17] Bairwa SK, Sonera SA, Tandel RC. Cholesterol based mesogenic Schiff's base derivatives with carbonate linkage: Synthesis, characterisation and photoluminescence study. Liquid Crystals. 2023;**50**:2495–2509.

[18] Huang H, Cong Y, Du A, et al. Liquid crystalline dimers containing a cholesteryl group: Chiral smectic phases, and re-entrant TGBA* phase. Journal of Molecular Liquids. 2022;**346**:117920.

[19] Lee H-C, Lu Z, Henderson PA, et al. Cholesteryl-based liquid crystal dimers containing a sulfur–sulfur link in the flexible spacer. Liq Cryst. 2012;**39**:259–268.

[20] Donaldson T, Staesche H, Lu ZB, et al. Symmetric and non-symmetric chiral liquid crystal dimers. Liquid Crystals. 2010;**37**:1097–1110.

[21] Al-shargabi A, Yeap G-Y, Mahmood WAK, et al. Liquid crystal dimers containing Cholesteryl and Triazole-containing mesogenic units. Liquid Crystals. 2020;**47**:219–230.

[22] Yeap G-Y, Alshargabi A, Mahmood WAK, et al. Synthesis, characterization and molecular organization for induced smectic phase of triazole ring in non-symmetric liquid crystalline dimer. Tetrahedron. 2015;**71**:3939–3945.

[23] Ooi Y-H, Yeap G-Y. λ-Shaped liquid crystal trimers with dual terminal cholesteryl moieties: synthesis and concomitant of N*, SmA and cholesteric glassy phases. Liquid Crystals. 2018;**45**:204–218.

[24] Donaldson T, Henderson PA, Achard MF, et al. Chiral liquid crystal tetramers. J Mater Chem. 2011;**21**:10935–10941.

[25] Majumdar KC, Ponra S, Chakravorty S. Synthesis and Characterization of Cholesterol-Based Tetramers. Molecular Crystals and Liquid Crystals. 2010;**528**:113–119.

[26] Liu X, Guo Z, Xie Y, et al. Synthesis and liquid crystal behavior of new side chain aliphatic polycarbonates based on cholesterol. Journal of Molecular Liquids. 2018;**259**:350–358.

[27] Hamley IW, Castelletto V, Parras P, et al. Ordering on multiple lengthscales in a series of side group liquid crystal block copolymers containing a cholesteryl-based mesogen. Soft Matter. 2005;**1**:355–363.

[28] Zhou Y, Briand VA, Sharma N, et al. Polymers Comprising Cholesterol: Synthesis, Self-Assembly, and Applications. Materials. 2009;**2**:636–660.

[29] Criswell TR, Klanderman BH, Batesky DC. Alkyl Carbonato Terminally Substituted Anils. Molecular Crystals and Liquid Crystals. 1973;**22**:211–238.

[30] Thaker BT, Dhimmar YT, Patel BS, et al. Studies of Calamitic Liquid Crystalline Compounds Involving Ester-Azo Central Linkages with a Biphenyl Moiety. Molecular Crystals and Liquid Crystals. 2011;**548**:172–191.

[31] The Nematic and Cholesteric Phases. Textures of Liquid Crystals [Internet]. John Wiley & Sons, Ltd; 2003. p. 51–74. Available from: https://onlinelibrary.wiley.com/doi/abs/10.1002/3527602054.ch5.

[32] DIERKING I. A review of textures of the TGBA* phase under different anchoring geometries. Liquid Crystals. 1999;**26**:83–95.

[33] Bairwa SK, Sonera SA, Tandel RC. Mesomorphic behaviour and photoluminescence study of novel homologous series of Schiff's base derived from cholesteryl carbonate and thiadiazole moiety. Liquid Crystals. 2024;**0**:1–14. doi: 10.1080/02678292.2024.2319631

[34] Imrie CT, Taylor L. The preparation and properties of low molar mass liquid crystals possessing lateral alkyl chains. Liquid Crystals. 1989;**6**:1–10.

[35] Date RW, Imrie CT, Luckhurst GR, et al. Smectogenic dimeric liquid crystals. The preparation and properties of the α,ω-bis(4- *n* -alkylanilinebenzylidine-4′-oxy)alkanes. Liquid Crystals. 1992;**12**:203–238.

[36] Ha S-T, Yeap G-Y, Boey P-L. Mesomorphic properties of biphenyl derivatives with cholesteryl moiety. IJPS. 2010;**5**:2185–2192.

[37] Kumarasamy Y, Byres M, Cox PJ, et al. Screening seeds of some Scottish plants for free radical scavenging activity. Phytotherapy Research. 2007;**21**:615–621.

[38] Westphal E, Bechtold IH, Gallardo H. Synthesis and Optical/Thermal Behavior of New Azo Photoisomerizable Discotic Liquid Crystals. Macromolecules. 2010;**43**:1319–1328.

[39] Madiahlagan E, B n S, Ngaini Z, et al. Synthesis, liquid crystalline properties and photo switching properties of coumarin-azo bearing aliphatic chains: Application in optical storage devices. Journal of Molecular Liquids. 2019;**292**:111328.

[40] Zhang R, Zhang Z, Han J, et al. Advanced liquid crystal-based switchable optical devices for light protection applications: principles and strategies. Light Sci Appl. 2023;**12**:11.

[41] Frisch M, Trucks G, Schlegel H, et al. Gaussian 09 (Revision A02). Gaussian Inc Wallingford CT. 2009;

[42] Pearson RG. Chemical hardness and the electronic chemical potential. Inorganica Chimica Acta. 1992;**198–200**:781–786.